Article

Patterns

# Multivariate hyperspectral data analytics across length scales to probe compositional, phase, and strain heterogeneities in electrode materials

## Graphical abstract

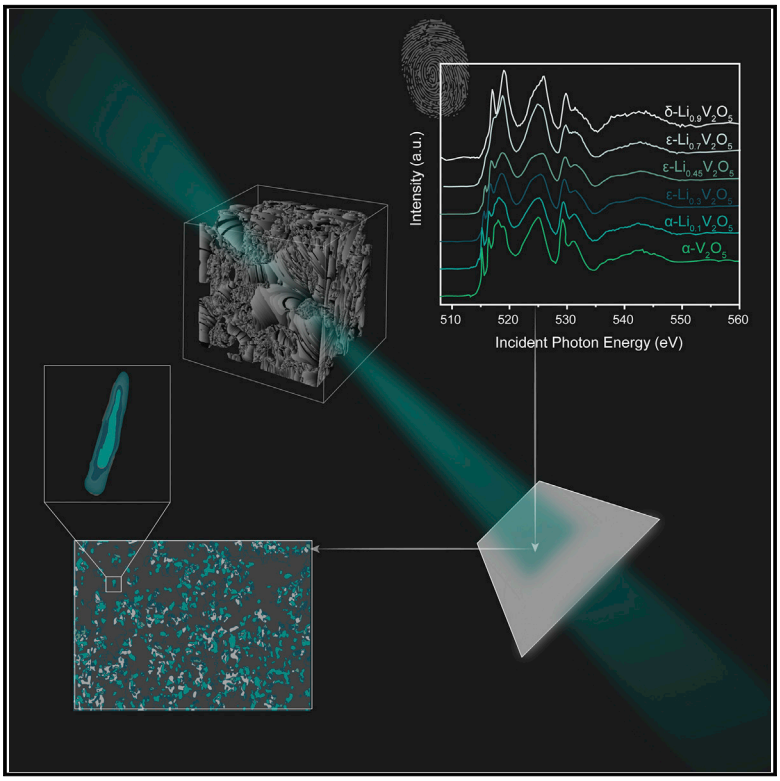


## Highlights

- Phase inhomogeneities and stress gradients govern electrode performance in batteries
- Hyperspectral imaging allows for the mapping of compositional variations
- Spectral databases are critical to investigating compositional heterogeneities
- Chemistry-geometry-mechanics coupling is crucial to lithiation phenomena

## Authors

David A. Santos, Justin L. Andrews, Binbin Lin, ..., Yu Ding, Bai-Xiang Xu, Sarbajit Banerjee

## Correspondence

justin.andrews@chem.tamu.edu (J.L.A.), xu@mfm.tu-darmstadt.de (B.-X.X.), banerjee@chem.tamu.edu (S.B.)

## In brief

In battery electrode materials, compositional heterogeneities give rise to stress gradients that ultimately result in degenerative failure. Progress in hyperspectral imaging has enabled an unparalleled view of multiphysics processes. Data science methods hold promise for deciphering mechanistic understanding from high-dimensional data. In this work, the utility of X-ray spectromicroscopy coupled with multivariate data analytics is demonstrated through multi-scale investigation of intercalation phenomena in a canonical cathode material aided by curation of a spectral standards database.

Santos et al., 2022, Patterns *3*, 100634
December 9, 2022 
https://doi.org/10.1016/j.patter.2022.100634

CellPress

Patterns

CellPress
OPEN ACCESS

Article

# Multivariate hyperspectral data analytics across length scales to probe compositional, phase, and strain heterogeneities in electrode materials

David A. Santos,[1,2,5] Justin L. Andrews,[1,2,5,*] Binbin Lin,[3] Luis R. De Jesus,[1,2] Yuting Luo,[1,2] Savannah Pas,[1,2] Michelle A. Gross,[1,2] Luis Carillo,[1,2] Peter Stein,[3] Yu Ding,[4] Bai-Xiang Xu,[3,*] and Sarbajit Banerjee[1,2,6,*]

[1]Department of Chemistry, Texas A&M University, College Station, TX 77843-3255, USA

[2]Department of Materials Science and Engineering, Texas A&M University, College Station, TX 77843-3255, USA

[3]Institute of Materials Science, Mechanics of Functional Materials, Technische Universität Darmstadt, Otto-Berndt-Str. 3, 64287 Darmstadt, Germany

[4]Department of Industrial and Systems Engineering, Texas A&M University, College Station, TX 77843-3255, USA

[5]These authors contributed equally

[6]Lead contact

*Correspondence: justin.andrews@chem.tamu.edu (J.L.A.), xu@mfm.tu-darmstadt.de (B.-X.X.), banerjee@chem.tamu.edu (S.B.)

https://doi.org/10.1016/j.patter.2022.100634

**THE BIGGER PICTURE** In battery electrode materials, phase inhomogeneities and stress gradients substantially influence battery performance and longevity. In this work, multivariate hyperspectral X-ray spectromicroscopy measurements are coupled with data dimensionality reduction and clustering techniques in conjunction with a spectral database and finite element analysis to probe compositional, phase, and strain heterogeneities in a canonical electrode material. The resulting maps are based on physically interpretable spectral standards and allow a detailed view of Li-intercalation-induced changes in the crystal lattice and electronic structure across decades of length scales. Direct observation of these changes across length scales provides a foundational understanding of lithiation processes and informs the design of next-generation electrode materials.


**Development/Pre-production:** Data science output has been rolled out/validated across multiple domains/problems

## SUMMARY

The origins of performance degradation in batteries can be traced to atomistic phenomena, accumulated at mesoscale dimensions, and compounded up to the level of electrode architectures. Hyperspectral X-ray spectromicroscopy techniques allow for the mapping of compositional variations, and phase separation across length scales with high spatial and energy resolution. We demonstrate the design of workflows combining singular value decomposition, principal-component analysis, k-means clustering, and linear combination fitting, in conjunction with a curated spectral database, to develop high-accuracy quantitative compositional maps of the effective depth of discharge across individual positive electrode particles and ensembles of particles. Using curated reference spectra, accurate and quantitative mapping of inter- and intraparticle compositional heterogeneities, phase separation, and stress gradients is achieved for a canonical phase-transforming positive electrode material, $\alpha$-$V_2O_5$. Phase maps from single-particle measurements are used to reconstruct directional stress profiles showcasing the distinctive insights accessible from a standards-informed application of high-dimensional chemical imaging.

## INTRODUCTION

Lithium-ion (Li-ion) batteries have expanded from consumer electronics to become a mainstay in electromobility applications and are starting to claim a growing share of the grid-level storage market.[1,2] The stringent performance and safety requirements of medium- and large-area energy storage formats have spurred a greater focus on the atomistic mechanisms and multiphysics

coupling underpinning degradation phenomena.[3–6] In many cases, the origins of performance degradation are traceable to multi-field and multiphysics coupling originating at atomistic scales, manifested at mesoscale dimensions, and compounded up to the level of electrode architectures.[7] A detailed understanding of electrochemistry-mechanics coupling and resulting emergent phenomena across many decades of length scales is imperative to unlock unexploited performance from existing battery chemistries, develop dynamic process controls, and design next-generation materials and architectures that are purpose-built to alleviate common modes of degradation.[8]

Degenerative capacity loss in batteries can derive from many sources, including loss of active material, stoichiometric drift, SEI formation, and rising internal resistance.[7,9] For the active electrode components of Li-ion batteries, mechanical stresses developed during electrochemical cycling play a key role in many degradation mechanisms. The accumulation of stress underpins delamination, crack formation, exfoliation, and even accelerated dissolution/migration reactions at interfaces.[7,10] In insertion electrodes, the insertion (extraction) of Li-ions drives successive dilation (contraction) of the host framework.[11,12] The close coupling between mechanics and electrochemistry plays an especially prominent role in phase-transforming electrode materials. In these materials, intercalation gives rise to multiphase coexistence regimes, which result in significant coherency strains at the interfaces between differently lithiated phases.[13,14] Direct observations of phase separation demonstrate a hierarchy of lithiation heterogeneities at the single-particle level, which are propagated across extended length scales, resulting in increased interfacial resistance, degraded rate performance, and loss of effective capacity.[9,12] Despite a growing appreciation of the link between lithiation inhomogeneities and battery degradation,[15,16] the mechanisms governing electrochemistry-mechanics coupling remains underexplored, especially with regard to localized phenomena.[17] A primary impediment lies in probing these processes with adequate resolution and chemical sensitivity across length scales.[18,19]

Increasingly, state-of-the-art electron microscopy and X-ray spectromicroscopy methods are being used to probe these processes using various contrast methods.[18,20] At the micron and nanometer length scale, for example, cross-section analyses of diffracted electrons from electron backscatter diffraction demonstrate the role of grain orientation on electrode degradation.[21] At the atomic scale, the transmission of electrons through electrode materials has been used to measure structural changes during cycling using transmission-electron microscopy.[22] In X-ray spectromicroscopy, brilliant and highly tunable X-rays from a synchrotron source are used to map pixel/voxel-wise X-ray absorption signatures across a heterogeneous sample[18] affording insights into the composition and critical atomistic and geometric correlators of intercalation phenomena.[23–27] Compared with electron microscopy, X-ray methods offer high penetration power and a significant degree of tunability (enabling the collection of chemical information over a range of length scales) while minimizing sample damage.[18,28] In a typical X-ray spectromicroscopy experiment, transmission intensities are recorded for a predefined field of view (typically between 4 and 100 $\mu m^2$) over one or more elemental X-ray absorption edges; this technique thus provides spatially resolved chemical information with element and orbital specificity.[29] A representative spectromicroscopy dataset can comprise as many as 1 million individual spectra and 250 images containing complex information about the chemical properties of a material mapped with nanometer-scale spatial resolution. A key challenge is thus to extract from these complex datasets a chemically intuitive understanding of compositional heterogeneities and their relation to particle dimensions and geometry.[16,24,30,31] A critical imperative for understanding degradation mechanisms is to map compositional variations to resulting stress gradients. Thus, for X-ray spectromicroscopy measurements that rely on absorption contrast, stress information needs to be derived from compositional gradients extrapolating from known structure parameters and stress tensors. Statistical regression and machine learning approaches hold promise for more effective utilization of hyperspectral datasets to correlate observed lithiation heterogeneities to geometric features and for the reconstruction of stress gradients. However, it is essential that such approaches be grounded in a physically meaningful interpretation of X-ray absorption spectra.

In this article, we demonstrate a workflow wherein multivariate statistical methods are used in conjunction with a library of reference spectra curated for samples with well-defined extents of lithiation to develop accurate chemical maps of lithiation gradients within individual particles and across ensembles of particles. At the individual particle level, composition maps from scanning transmission X-ray microscopy (STXM) and X-ray ptychography are further correlated with stress gradients with the help of finite element analysis (FEA). Using orthorhombic $V_2O_5$ as a model system,[32,33] we examine phase evolution upon Li-ion intercalation and construct a library of X-ray absorption standards for samples that have been rigorously characterized by multimodal methods. By combining statistical approaches with curated reference spectra, we demonstrate a generalizable approach to composition, phase, and stress mapping, which provides critical insights into modulating battery chemistry and electrode architecture to alleviate common degradation mechanisms.[18,34,35]

## RESULTS AND DISCUSSION

### A curated X-ray absorption spectroscopy reference database for $Li_xV_2O_5$

Orthorhombic $\alpha$-$V_2O_5$ is a layered compound with multiple accessible redox couples ($V^{5+}/V^{4+}$ and $V^{4+}/V^{3+}$) and a framework that can support intercalation of up to three Li ions per formula unit (i.e., up to a final composition of $Li_3V_2O_5$).[36,37] The promise of this material as an intercalation electrode stems from a high theoretical capacity (up to 441 mAh/g) and the potential for multielectron redox.[32,33,37] A growing appreciation for the geographical diversity of vanadium deposits and the maturity of extraction methods with low-carbon footprints has driven further interest in $V_2O_5$ in light of growing concerns about greenhouse emissions from battery manufacturing and the resilience of supply chains.[38] Despite current use as a positive electrode (cathode) for small-format commercial cells, widespread adoption of $V_2O_5$ in larger formats has been stymied by a series of intercalation-induced phase transformations, which gives rise to stress and diffusion impediments and limits the accessible energy density and cycle life.[32,35,39] Thus, while

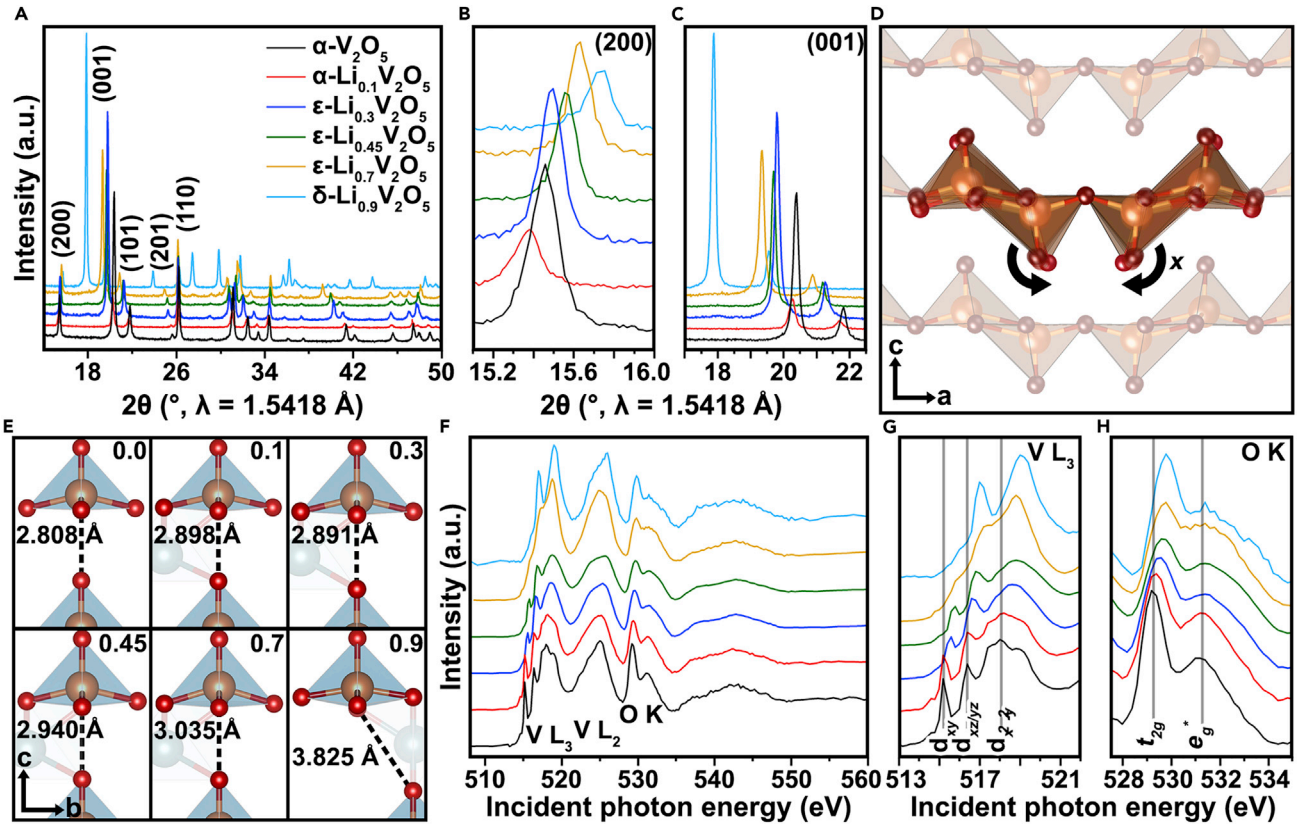


**Figure 1. Li-ion intercalation-induced evolution of crystal lattice and electronic structure**

(A–C) (A) Powder X-ray diffraction patterns collected for phase-pure stoichiometric $Li_xV_2O_5$ materials demonstrate intercalation-induced (B) contraction of the lattice along the a axis and (C) expansion of the lattice along the b axis. Rietveld refinement of the powder diffraction data shown in (A) is shown in Figure S1. Structure solutions obtained by Rietveld refinement are shown in Figure S2.

(D) Li-ion intercalation further induces monotonically increasing canting of the apical oxygens toward the intercalated lithium-ion and puckering of the $V_2O_5$ layers (Figure S3).

(E) Finally, the $VO_{5+1}$ quasi-octahedron evolves as the sixth long bond gradually lengthens. In the highly lithiated δ-phase, a half-layer shift in the ab plane gives rise to a purely $VO_5$ square pyramid coordination environment.

(F) Closely overlapping V L- and O K-edge X-ray absorption spectra obtained by analysis of STXM data for individual particles (Figures S4 and S5) demonstrate lithiation-induced modification of local coordination environments.

(G and H) Expanded regions of the (G) V $L_3$- and (H) O K-edges are provided. Shifts of absorption features to higher energies and a monotonic diminution in the intensity of pre-edge features are demonstrated with increasing lithiation. Linear curve fitting of these spectra is shown in Figures S6 and S7.

specific emphasis is placed on the methodology of interpreting hyperspectral imaging data in this work, in light of increasing material criticality challenges faced by incumbent positive electrode chemistries, the insights obtained here the role of defects and particle geometry on electrochemistry-mechanics coupling in $V_2O_5$ have practical implications for next-generation batteries.[32,40]

To develop a rigorous set of standard X-ray absorption spectra for use in hyperspectral image analysis, phase-pure $Li_xV_2O_5$ materials (where $x$ denotes the extent of lithiation) were prepared by reacting $V_2O_5$ powders with stoichiometric amounts of lithium iodide (LiI), as described in the experimental procedures.[24] As $V_2O_5$ incorporates Li, its crystal lattice and electronic structure are strongly modified, as shown in Figure 1.[12] Powder X-ray diffraction (PXRD) patterns for each phase are shown in Figure 1A, and the corresponding Rietveld refinements and structure solutions are shown in Figures S1 and S2, respectively. Tables S1–S6 show the Rietveld refinement statistics and atom positions; the evolution of lattice parameters is summarized in Table S7. Upon intercalation, $V_2O_5$ undergoes several discontinuous changes to its crystal structure, stabilizing α-, ε-, and δ-phases with increasing lithiation, corresponding to lithium stoichiometries of ca. $0.0 < x < 0.1$, $0.3 < x < 0.7$, and $0.9 < x < 1.0$, respectively.[34] With the exception of the highly lithiated δ-phase, which necessitates a half-layer shift in the ab plane (Figure 1E), contraction of the lattice along the a axis, and expansion of the lattice along the b axis can be observed with increasing lithiation, as shown in Figures 1B and 1C, respectively. With increasing lithium content, electron density becomes localized on specific vanadium sites, the nearest apical oxygens become canted toward intercalated lithium-ions (Figure 1D), and the $V_2O_5$ layers are increasingly puckered (Figure S3; Table S8).[41] These profound changes in bonding motifs coupled with the structural distortions give rise to inhomogeneous stress gradients as a result of anisotropic lattice contraction and expansion along different crystallographic directions.

The phase transformations and changes in lattice symmetry observed by XRD are accompanied by changes in local vanadium and lithium coordination environments. These alterations are demonstrated in X-ray absorption near-edge structure (XANES) spectra, which depend sensitively on the local coordination geometry and ligand field. Interpretation of XANES spectra is complicated by multiplet effects, known limitations of density functional theory in predicting the electronic structure of complex oxides,[42,43] and challenges in treating core holes.[44] First-principles approximations, including multiple scattering,[45] time-dependent density functional theory,[46] local pair natural orbital coupled cluster methods,[47] and self-consistent-field methods coupled with many-body perturbation theory,[44] have been used to simulate XANES spectra with varying degrees of success. First-principles approximations provide insight into the physical origins of spectral features but accurate treatments of core holes are often challenging to implement for many-body correlated systems, such as typical positive electrode materials, especially upon incorporation of defects and alloying. We present here a database of experimental spectra derived from STXM measurements (Figure 1F) acquired across V L- and O K-edges of phase-pure individual particles of α-, ε-, and δ-$Li_xV_2O_5$ (Figures S4). Principal-component and k-means clustering analyses have been performed for each measurement to validate the phase purity of the samples, as shown in Figure S5. The spectra in Figure 1F can thus be unambiguously assigned as spectral signatures of the differently lithiated phases with variations manifested in Figure S5 solely from detector nonlinearity at higher thicknesses.

## Evolution of spectral features at V L- and O K-edges as a function of lithiation

As shown in Figure 1F, the V L-edge (~510–525 eV) comprises two dominant features centered at ~518 (V $L_3$) and ~525 eV (V $L_2$). The V $L_2$-edge results from transitions from V $2p_{1/2}$ → V 3d states and remains relatively consistent across all phases. A Coster-Kronig Auger emission process that broadens spectral features limits the value of this absorption feature as a fingerprint of lithiation-induced changes in local structure.[48] In contrast, the V $L_3$-edge (Figure 1G), which corresponds to transitions from V $2p_{3/2}$ core states → V 3d states, offers a wealth of information. Fine features centered near 515 and 517 eV correspond to V 2p → V $3d_{xy}$ and V 2p → V $3d_{xz/yz}$ transitions, respectively.[47,49] Li-ion intercalation into $V_2O_5$ results in a formal reduction of the vanadium centers, which shifts the $d_{xy}$ and $d_{xz/yz}$ features to higher energies (Figure S6; Tables S9–S12). Since XANES probes the unoccupied density of states (i.e., the conduction band), a diminution of the $d_{xy}$ and $d_{xz/yz}$ intensities is observed due to Pauli blocking as V 3d states are filled with increasing lithiation.

The relative intensities of the $t_{2g}$ and $e_g$* features in O K-edge XANES spectra in Figure 1H are also greatly modulated by the lithiation extent. With increasing lithiation, the $t_{2g}$ feature is diminished in intensity with respect to the $e_g$* absorption. This modulation of relative intensities is a consequence of electron correlation (since lithiation introduces V $3d^1$ states), the loss of degeneracy between spin-up and spin-down states upon lithiation, and the concomitant reduction of vanadium centers (which modifies V 3d-O 2p hybridization), and the elongation and canting of V-O bonds (Figure S3; Table S8).[49] The changes in V-O hybridization cause a shift in the spectral weight of the $e_g$* and O 2p-V 4sp hybridized states to higher energies (Figure S7; Tables S9–S11 and S13). Notably, the pronounced structural rearrangement across the ε↔δ phase transition does not follow this trend. Instead, a shift from a distorted octahedral (i.e., $VO_{5+1}$ environment) to an unambiguously square pyramidal coordination results in a change in the crystal field splitting marked by a re-emergence of a sharp $3d_{xz/yz}$ feature centered near 517 eV at the V $L_3$-edge and renormalization of the $t_{2g}$-to-$e_g$* intensity at the O K-edge.

## Using reference spectra to guide composition and phase mapping by X-ray spectromicroscopy

Access to validated reference $Li_xV_2O_5$ XANES spectra (Figure 1) enables accurate and efficient interpretation of lithiation heterogeneities imaged by high-dimensional X-ray imaging techniques, such as STXM and X-ray ptychography. In STXM, transmission images are obtained over a series of image positions, $p = 1 \ldots P$, along a series of energies $n = 1 \ldots N$. During pre-processing, the incident flux $I_0$ is utilized to calculate an optical density matrix to establish a linear relationship between the absorption coefficient (μ), which is dependent on the extent of lithiation and thickness ($t$).[29] For a heterogeneous sample comprising a set $s = 1 \ldots S$ number of spectroscopically distinct constituents, the optical density, $D_{N\times P}$, can be expressed as a spectrum for each pixel as:

$$D_{N\times P} = \mu_{N\times S} \cdot t_{S\times P}, \quad \text{(Equation 1)}$$

where $\mu_{N\times S}$ represents the set of exact spectra for all the $s = 1 \ldots S$, and their corresponding weighting at every pixel is denoted by $t_{S\times P}$. Thus, provided $D_{N\times P}$ from X-ray spectromicroscopy measurements, the goal is to find solutions for the set of spectra ($\mu_{N\times S}$) and weighting maps ($t_{S\times P}$) which accurately represent the contributions of each component at individual pixels.[50] A workflow for these processes and the construction of stress maps is illustrated in Figure 2. When the exact set of absorption spectra ($\mu_{N\times S}$) is well defined, spectral maps ($t_{S\times P}$) can be obtained by matrix inversion using singular value decomposition (SVD) as follows:

$$t_{S\times P} = (\mu_{N\times S})^{-1} \cdot D_{N\times P}. \quad \text{(Equation 2)}$$

Furthermore, when spectral signatures are known for each composition, hyperspectral maps can be used to visualize composition gradients. This scheme, where $\mu_{N\times S}$ is directly defined using the curated spectral library acquired for standards, is described in this work as a direct deconvolution, which is represented in the overall workflow sketched in Figure 2 by the direction of the orange arrows. Alternatively, when a direct convolution with reference spectra is not possible (as a result of the presence of impurities, energy calibration errors, or excess noise), additional steps are required to find a solution for $\mu_{N\times S}$. An example of this scheme is represented in Figure 2 by the direction of the teal arrows (i.e., principal-component analysis [PCA] → reduced-dimensionality search space → cluster analysis → $\mu_{N\times S}$). A more detailed presentation of the matrix notation

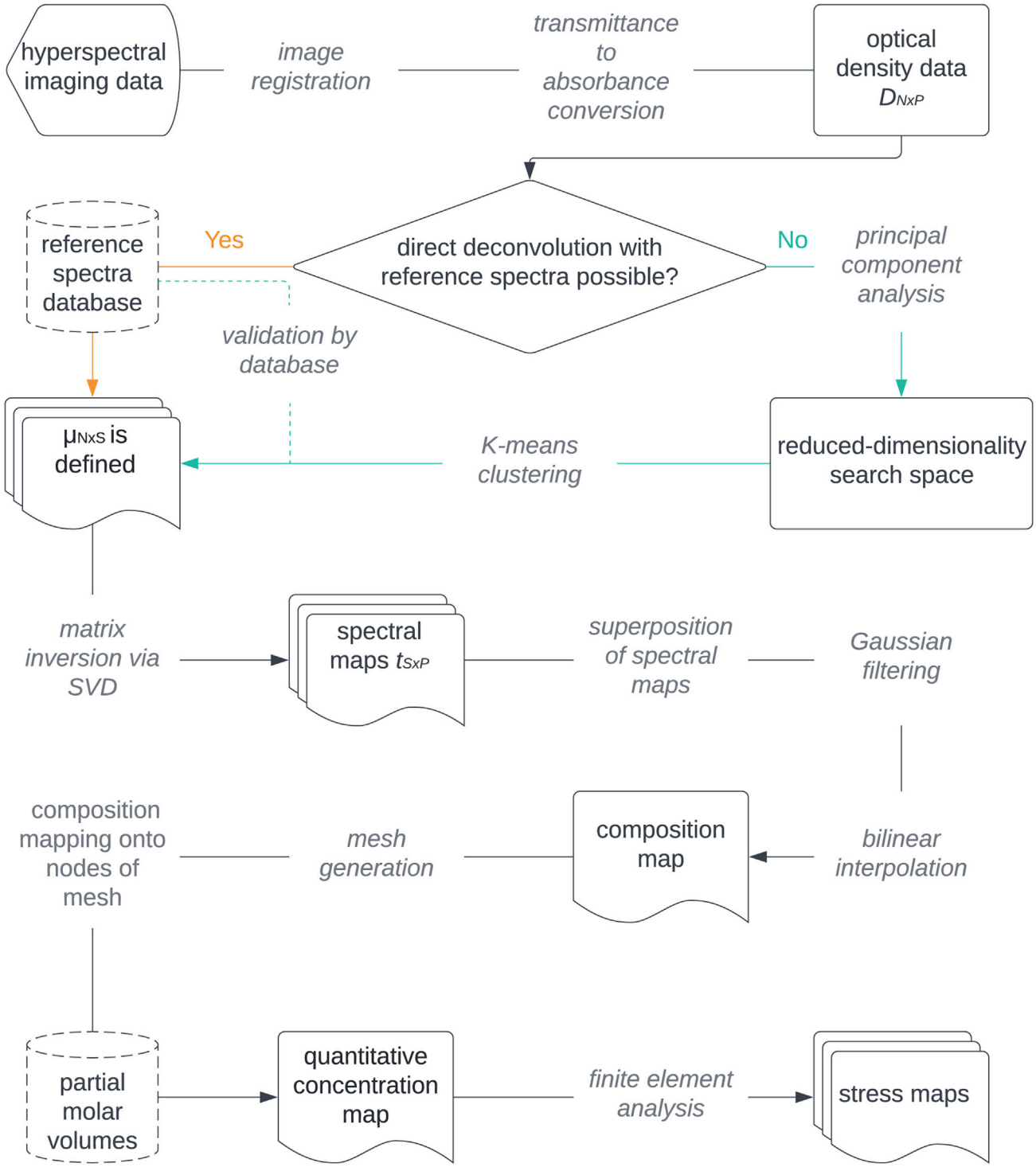


**Figure 2. Alternative workflows using reference spectra to generate composition and stress maps from hyperspectral imaging data**

A region of interest is imaged across a range of incident photon energies spanning one or more elemental absorption edges. A frame stack can be generated by appropriately aligning the images to account for beam drift and stacking them along the energy dimension. A background spectrum is utilized to transform transmission images to optical density data represented as a matrix, $D_{N\times P}$. If a direct analysis with reference spectra is possible, spectral maps can be generated by SVD (indicated by orange arrows). Alternatively, PCA can be utilized to aid cluster analyses of pixels based on spectral similarity; comparison of the cluster spectra against reference spectra informs accurate assignments of spectra to $Li_xV_2O_5$ phases (indicated by teal arrows). Composition maps can be further used to map intercalation-induced stresses by FEA to extract insight into electrochemistry-mechanics coupling. The latter is a purely physics-based calculation and solves for linear elastic mechanics in 2D.

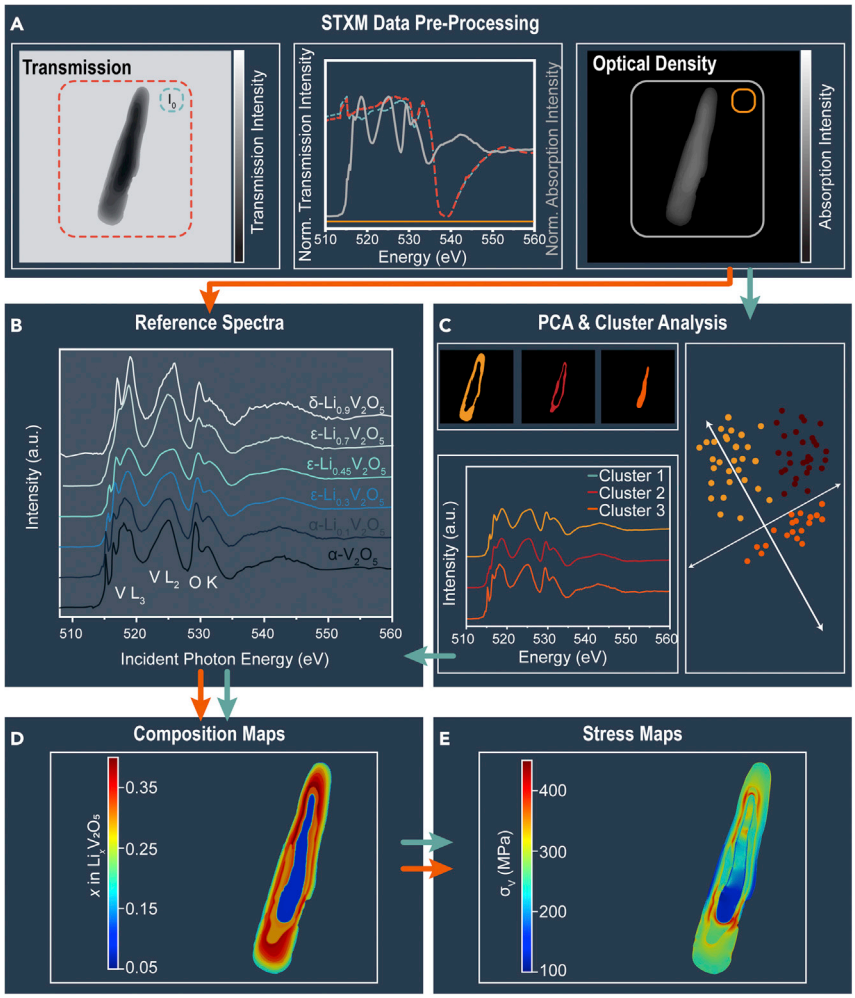


**Figure 3. A demonstrative workflow for generating composition and stress maps using an artificial STXM dataset**

(A) A frame stack can be generated by appropriately aligning the images to account for beam drift and stacking them along the energy dimension. A background spectrum (denoted as $I_o$ and highlighted by the teal dotted circle) is utilized to transform the data from transmission (left) to absorption (right), revealing the absorption profile of the sample (denoted by the white spectrum in the center panel).

(B) If accurate energy and intensity calibrated spectra are readily available, composition maps can be generated by SVD (workflow indicated by orange arrows).

(C) Alternatively, PCA can be utilized to cluster regions based on spectral similarity; comparison of the cluster spectra against reference spectra informs accurate assignments of spectra to $Li_xV_2O_5$ phases (workflow indicated by teal arrows).

(D) Quantitative composition maps can be generated by superimposing spectral maps generated by an SVD using normalized spectra corresponding to a known lithium stoichiometry.

(E) Composition maps can be further used to quantify intercalation-induced von Mises stress profiles by FEA to extract insight into electrochemistry-mechanics coupling within individual particles. The latter is a purely physics-based calculation and solves for linear elastic mechanics in two dimensions.

for this process is available from Lerotic et al.[50,51] and Koprinarov et al.[52]

Initially, we describe these approaches using the synthetic dataset shown in Figure 3A to facilitate discussion and validation of each methodology. In particular, we seek to effectively utilize the measured spectral signatures of distinctly lithiated phases (Figure 3B) to develop a transparent and physically meaningful framework for interpreting large hyperspectral datasets. The synthetic dataset shown in Figure 3A consists of three spectroscopically distinct (Figure S8) regions comprising phase-pure $\alpha$-$Li_{0.1}V_2O_5$ and $\varepsilon$-$Li_{0.45}V_2O_5$ in addition to a $Li_{0.35}V_2O_5$ $\alpha/\varepsilon$ phase mixture oriented in a core-shell motif,[53] a common multiphasic lithiation pattern observed during ion intercalation. In a direct deconvolution of the synthetic dataset, a set of images ($t_{S\times P}$) representing the weighting of each spectrum in the sample (Figure S9), is obtained by SVD as described in Equation 2, wherein $\mu_{N\times S}$ has been defined using the library of XANES standards. When plotted using a uniform grayscale, the spectral maps corresponding to the phases present in the dataset are clearly represented (S9B and S9D) in sharp contrast to the remaining spectral maps corresponding to $V_2O_5$ phases that are not present in the sample (S9A, S9C, S9E, and S9F). In this example, spectral maps are calculated for the entire library of XANES spectra, and the relative weightings of each component are used to deduce which phases are present in the sample. As shown in the composition map in Figure 3D, this approach captures the artificial dataset's ground-truth, a core-shell phase separation motif, with excellent fidelity (Figure S8). It is worth noting, however, that prior knowledge about the sample, such as depth of discharge, can be utilized to narrow the selection of spectral signatures considered for SVD (i.e., to visualize the spatial orientation of known phases in the sample).

It is important to note here that the success of a direct deconvolution with standards stems in some measure from the fact that the validation dataset was initially generated using reference spectra; this represents the best-case scenario wherein the input spectra used for deconvolution are an excellent match to the measured data. While the great utility of a direct analysis cannot be understated, a direct spectral deconvolution with standards comes with some caveats. For example, while the matrix inversion process described in Equation 2 can be applied to any combination of input spectra, the fidelity of the spectral maps depends strongly on the extent to which the reference spectra are a one-to-one representation of the measured data ($D_{N\times P}$).[52] Here, sample thicknesses above a certain threshold (inducing nonlinearities), parasitic reactions generating non-vanadium oxide phases, environmental noise, errors in the energy calibration, potentially polarization dependences of spectral intensities arising from particle orientation,[54] and contributions

from the halo of the incident beam can lead to erroneous results. An illustration of this is provided in Figure S10, which shows invalid results produced by a direct SVD, using the library of standards applied to a modified dataset incorporating a −0.4 eV energy calibration error and the addition of Gaussian noise.[55] One approach to minimize this limitation is a collection of internal standards from known phase-pure regions; however, the complexity of this approach greatly increases with the number of chemical constituents. In this work, a considerable amount of effort has been placed on minimizing many of these sources of error during data collection, for example, by limiting sample thickness and mitigating the formation of non-vanadium oxide phases, as discussed in the experimental procedures.

We have examined an alternative approach to analyzing hyperspectral datasets acquired for complex samples, which is the most likely scenario for realistic energy storage materials. This approach, illustrated by the direction of the teal arrows in Figures 2 and 3, fuses knowledge of standards (Figure 3B) with PCA and cluster analysis (Figure 3C) to find spectroscopically similar groupings of data that represent distinct $Li_xV_2O_5$ phases. The first step in this approach aims to provide a reduced dimensionality search space that retains all of the meaningful variations in the data—this can be accomplished by PCA, as shown in Figure S11. Next, pixels with similar spectral signatures can be grouped according to their Euclidean distance in the eigenvector search-space provided by PCA; here, the average spectral response of every pixel belonging to a cluster can be used to define the set of spectra, $\mu_{N\times S}$, as shown in Figure S12 for the test set. In this approach, the number of selected principal components and clusters is user adjustable and critical to an accurate determination of $\mu_{N\times S}$. Without access to standards, selecting the number of principal components can be aided by referencing their cumulative variance.[50] Indeed, as shown in Figure S11 for the test dataset, the majority of the variance in the data is captured by the first few components (>99.9% from the first two components in the test set). Subsequently, during clustering analyses, color-coded scatterplots of clusters, as shown in Figure S12A, can be utilized to investigate how clusters are separated in eigenvector space to inform the number of user-selected clusters that form $\mu_{N\times S}$. In an ideal execution of k-means clustering via PCA, the number of partitions and their spectral identity should match the chemically distinctive constituents present in the sample (contrast Figure S8 with Figure S12)—in practice, this can be difficult to achieve by solely monitoring the statistical properties of the data. In this work, signatures of the eigenspectra (which are often reminiscent of the difference spectra between standards) and cluster spectra are validated using the library of X-ray absorption standards to enable an electronic-structure-informed selection of the number of principal components and clusters selected for $\mu_{N\times S}$. Figures S11 and S12 show that this supervised approach, guided by standards to PCA and clustering, respectively, can successfully partition data based on spectral similarities to obtain a set of spectra ($\mu_{N\times S}$), even in the presence of Gaussian noise and energy misalignment in the modified dataset.[56] A combined PCA and k-means clustering approach thus represents a powerful means of determining $\mu_{N\times S}$ of the spectral components based on statistical deconvolution of datasets.[50,52,57,58] Notably, the cluster analysis in Figure S12 delineates three distinct clusters despite the presence of only two $Li_xV_2O_5$ phases in the generated dataset. These results thus highlight a crucial distinction between direct deconvolution aided by spectral standards and deconvolution based on clustered spectra. The former can disentangle the individual contributions of multiple phases. In contrast, the latter must assign regions of mixed composition to either a separate cluster or as part of a closely related cluster. One approach to resolving this uncertainty is to over-cluster the data to achieve greater segmentation and enable interactive curation by analyzing dendrograms (based on Euclidian distance) or comparison with standards.[58,59] An additional method for refining the search space has been highlighted by Lerotic and co-workers, wherein cluster-similarity regularization is incorporated with non-negative matrix analysis to introduce a physically meaningful bias toward properties of known spectra.[60]

In all instances, it is crucial to be cognizant of each approach's limitations and monitor any residual errors to avoid erroneous results. Using PCA, for example, has been shown to produce negative weighting values, which are unphysical and represent a limitation to its utility for quantitative interpretation.[60] Although the fine spectral features of the X-ray absorption spectra provide the physical basis for distinguishing components in a heterogeneous material, spectra should be placed on an absolute mass-absorption scale to avoid fitting peak intensity differences stemming from thickness effects—this can introduce systematic errors resulting from uncertainties in the mass-absorption coefficients.[52] These and other sources of error can be monitored by tracking residual maps (Figure S9G) and residual plots, as shown in a subsequent section. Whether employing a direct deconvolution of datasets using standards or a combined approach using PCA and cluster analysis, access to a library of reference spectra enables user-supervised validation to ensure physically meaningful interpretation of the data.

The spatially resolved weighting of each phase, either determined by direct deconvolution or abetted by the use of reference spectra and statistical methods, can be utilized to generate composition/concentration maps, providing a quantitative representation of the extent of lithiation (or depth of discharge in the case of electrochemically lithiated samples).[35] To reduce noise and enable a continuous representation of the data, spectral maps are subjected to a Gaussian filter and bilinear interpolation step (see experimental procedures). The reconstructed composition map for the test particle, shown in Figure 3D, thus reproduces the spatial localization of the $\alpha$-$Li_{0.1}V_2O_5$ and $\varepsilon$-$Li_{0.45}V_2O_5$ phases, their phase mixtures, and the relative thickness gradient within the particle (Figure S8) with fine detail and excellent fidelity to the original dataset. Figure 3E shows von Mises stress values obtained for the test particle by translating composition gradients to stress via FEA as described in the supplemental experimental procedures.[24,34] The process of translating composition maps to stress gradients is physics-based and involves FE calculations, solving 2D linear elastic mechanics with corresponding boundary conditions. The commonly used von Mises stress (2D) criterion is applied to compute an equivalent stress of the Cauchy stress tensor at every point within the particle, thereby providing a snapshot of the overall stress state resulting from lithiation heterogeneities.[61]

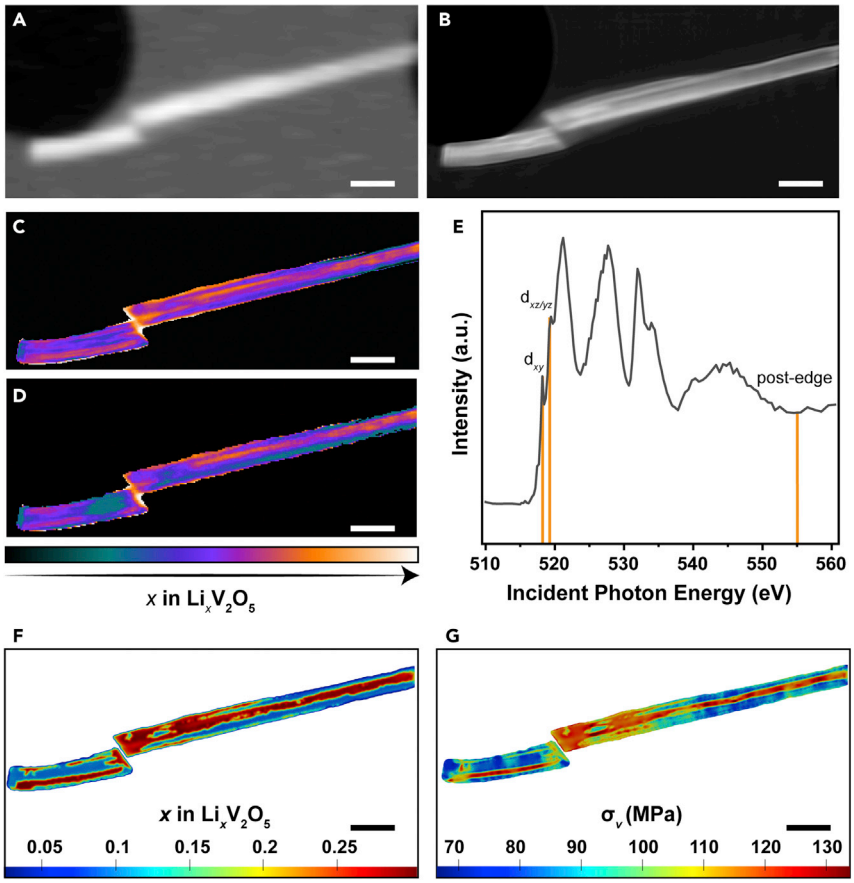


**Figure 4. Analysis of single-particle lithiation heterogeneities by STXM and X-ray ptychography**

(A and B) Optical density maps from STXM (A) and X-ray ptychography (B) at 518.2 eV, contrasting differences in spatial resolution and chemical contrast between the two hyperspectral spectromicroscopy techniques.

(C–E) Lithiation maps from ptychography images collected at 518.2 and 519.4 eV are shown in (C and D), respectively, based on the relative intensity of the $d_{xy}$ and $d_{xz/yz}$ features as marked in the integrated STXM spectrum across V L- and O K-edges in (E).

(F and G) The composition map shown in (F) was generated by mapping the experimentally determined lithiation gradients to a Gaussian filter-smoothed image, which informed the calculation of von Mises stress profiles as shown in (G) for fixed boundary conditions. Scale bars, 500 nm.

In general, regions of high von Mises stress correlate with highly lithiated domains as a result of compressive stresses. The most significant stress experienced by the test particle coincides with phase boundaries, reflecting the sharp changes in lithiation and elastic misfit strain at the $\alpha$-$Li_{0.1}V_2O_5$ and $\varepsilon$-$Li_{0.45}V_2O_5$ interface.[62] A complete picture of lithiation-induced stresses is provided in Figure S13, wherein the complex stress state is deconvoluted into the von Mises, normal, and shear stress components under fixed and free boundary conditions. Here, the choice of boundary conditions is intended to capture the likely varying interactions, in a real electrode, between the active primary particles and the surrounding electrode, which can significantly influence the stress state of a given particle. It is important to note here that, while linear elasticity does not directly predict fracture, it provides an overall snapshot of the stress state, which captures the intercalation-induced stresses that typically precede failure.[10,63] Delineation of displacement, von Mises stress, nominal stress along $\xi$, nominal stress along $\eta$, and shear stress for free boundary conditions and fixed boundary conditions in Figure S13 provides an unprecedented view of chemistry-mechanics coupling in insertion cathodes.

In summary, we have demonstrated that spectral standards can enable accurate chemical mapping using a synthetic hyperspectral dataset generated from reference spectra. In the absence of spectral contamination, reference spectra can be used directly to deconvolute contributions from different phases within a heterogeneous sample. Alternatively, reference spectra enable a supervised approach to spectral deconvolution in conjunction with statistical clustering approaches in a more general scenario. The composition maps generated from the accurate assignment of the spatial disposition of lithiated phases can furthermore be used to reconstruct a detailed picture of stress gradients within individual particles. We now focus on applying standards to experimental STXM data collected for heterogeneous $Li_xV_2O_5$ nanoparticle samples to demonstrate the utility of this approach. Phase distributions are investigated across length scales with the help of our curated reference spectra (Figure 1F). In subsequent sections, lithiation heterogeneities are mapped at the level of individual particles, small ensembles, and particle networks.

## Evaluating lithiation heterogeneities and stress gradients within individual particles

We start at the smallest length scale with hyperspectral data of the highest spatial resolution. The lithiated $V_2O_5$ nanowire fragments shown in Figure 4 were initially screened by STXM (Figure 4A) at 50 nm resolution and subsequently by X-ray ptychography at 10 nm resolution (Figure 4B). X-ray ptychography is a coherent diffraction imaging technique capable of making hyperspectral measurements, bearing resemblance to STXM as an element-specific probe, with marked improvements in spatial resolution,[27] as is readily apparent by contrasting Figure 4A (STXM) with 4B (ptychography). As a lens-less technique, the spatial resolution of X-ray ptychography is limited only by the wavelength of the incident photon energy.[64] Given the massive datasets generated by spectroptychography (on the order of terabytes), STXM can be utilized as a preliminary screen to identify a limited set of photon energies that best capture chemical contrast. Figures 4C and 4D show ptychography maps constructed from coherent diffraction patterns at 518.2 and 519.4 eV, respectively, which correspond to the $d_{xy}$ and $d_{xz/yz}$

absorption features at the V $L_3$-edge as shown in the integrated absorption spectrum derived from STXM in Figure 4E. Optical density maps at 518.2 and 519.4 eV have been normalized by an optical density profile collected at the post-edge (555.0 eV) to eliminate mass thickness contrast. This enables the comparison of relative $d_{xy}$ and $d_{xz/yz}$ absorption intensities, which, as observed in Figure 1G, are powerful indicators of the extent of intercalation. The inferred lithiation gradients from individual $d_{xy}$ and $d_{xz/yz}$ images are consistent and broadly depict core-shell behavior wherein nanowire edges are sparsely lithiated relative to a Li-rich core. A linear combination fit (LCF) with energy-aligned standards has been performed on the STXM data to enable a more quantitative look at phase separation, as shown in Figure S14. The results from LCF indicate a nearly even mixture of $\alpha$-$Li_{0.1}V_2O_5$ and $\varepsilon$-$Li_{0.30}V_2O_5$. The concentration map shown in Figure 4F has been computed based on pixel intensities from Figure 4C (indicative of lithiation) within lower and upper bounds for lithiation set by the $\alpha$-$Li_{0.1}V_2O_5$ and $\varepsilon$-$Li_{0.30}V_2O_5$ phase. Notably, the tips of both nanowire fragments appear heavily lithiated, likely due to preferential nucleation at fragmented edges with a large density of defects, which lower the barrier to nucleation. The outstanding spatial resolution of X-ray ptychography enables visualization of additional Li-rich channels originating from the nanowire edges and running along the length of the nanowire fragments. Here, the insertion of lithium-ions between specific layers likely drives further insertion into the expanded layer, a phenomenon akin to staging,[49] thus driving preferential diffusion along locally expanded layers.

A high-resolution composition and phase map enables visualization of stress through finite element simulations, as shown in Figure 4G. Here, we primarily discuss the von Mises stress since it provides, at a glance, an expression of the overall stress state of the material. It should be noted here that stress values are calculated (not directly imaged) utilizing the composition map combined with knowledge of the partial molar volumes of the individual variously lithiated phases. The most significant regions of von Mises stress coincide with areas of high lithiation, reflecting the compressive strain induced by a locally expanded Li-rich core against a sparsely lithiated shell. Striations oriented perpendicular to the nanowire length are observed due to boundary constraints that account for additional compression or tension due to volumetric expansion or contraction against the substrate. Secondary areas of elevated von Mises stress coincide with highly lithiated nanowire tips; lithiation-induced local compression of the crystal lattice likely alters the local diffusion rate, exacerbating lithiation differences and driving additional coherency strain.[24,62] A full profile of stress calculations from FEA is shown in Figure S15—which provides a rich picture of lithiation-induced stress gradients. For the particle fragments shown in Figure 4, interparticle diffusion is limited, and the thermodynamic driving forces for phase separation are accommodated by intraparticle lithiation gradients.[24,25,34,65] Furthermore, defects at frayed nanoparticle tips strongly modify nucleation and subsequent phase propagation. As such, Figure 4 provides a compelling demonstration of the use of single-particle X-ray spectroscopy and X-ray ptychography aided by reference spectra to image phase separation with <10 nm spatial resolution. Future work will focus on acquiring and utilizing phase images provided by X-ray ptychography with greater spectral resolution to maximize contrast in individual particles and cross-sectioned single crystals.[66–68]

## Imaging particle-by-particle lithiation in small ensembles of $V_2O_5$ nanoparticles

We next turn our attention to a small ensemble of $V_2O_5$ nanoparticles to examine the role of interfaces between active electrode particles.[69,70] Figure 5 shows interparticle heterogeneity in two pairs of interfacing nanowires following "on-substrate" lithiation described in the experimental procedures.[34] This approach to chemical lithiation enables the investigation of interactions between adjacent or solid-solid interfaced particles during Li-ion insertion. The spatial resolution in Figures 5A and 5B is 30 and 50 nm, respectively, which is sufficient for investigating interparticle and intraparticle lithiation inhomogeneities. Spectral deconvolution by SVD reveals comparably low and high lithiated phases, demonstrating the strongly preferential lithiation of one particle at the expense of the other during early (Figure 5A) and later stages of lithiation (Figure 5B).

The spectrum for the low lithiated nanowire in Figure 5A (orange) is shown in Figure 5C and is characterized by sharp $d_{xy}$ and $d_{xz}/_{yz}$ features at the V $L_3$-edge, as well as a relatively strong $t_{2g}$ feature compared with the $e_g$* feature at the O K-edge. These features collectively suggest little-to-no lithium insertion. In contrast, the intensity of the $d_{xy}$ and $d_{xz}/_{yz}$ features in the light-blue spectrum is diminished and has broader lineshapes, indicating some reduction of the formal vanadium oxidation state. Furthermore, the O K-edge exhibits a lower $t_{2g}$-to-$e_g$* ratio, demonstrating a relatively higher degree of lithiation. Particle-by-particle lithiation is driven by a strong energetic preference for diffusion across an interface, which is preferred over nucleation of a lithiated phase.[69] Analogous mosaic instabilities have been modeled by Delmas et al.[71] and experimentally shown by Chueh et al.[26] for another phase-separating positive electrode material, $Li_xFePO_4$. This mechanism is characterized by phase coexistence within particle ensembles but not within single particles since diffusion across interconnected particles can mitigate the formation of phase boundaries. Indeed, PCA and k-means clustering analysis performed for isolated segments from each nanowire suggest little-to-no intraparticle lithiation heterogeneities (Figure S16).

Unlike $LiFePO_4$, which has a singular miscibility gap and shows two-phase separation between Li-rich and Li-poor phases,[26,72,73] lithiation of orthorhombic $V_2O_5$ progresses through a sequence of $Li_xV_2O_5$ phases (Figures 1 and S17), thereby introducing multiple energetic barriers for phase nucleation. The spectrum shown in Figure 5D for the lowly lithiated nanowire (yellow, Figure 5B) is most similar to the $\varepsilon$-$Li_{0.3}V_2O_5$ phase. In sharp contrast, the adjacent particle (blue) shows a much greater extent of lithiation corresponding to $\delta$-$Li_{0.9}V_2O_5$. Notably, lithiation beyond $x > 1$ in $V_2O_5$ leads to the irreversible formation of a $\gamma$-phase requiring considerable distortion and inversion of the square pyramids in addition to the sliding of layers.[69,74] Here, in a particle-by-particle sequence of lithiation, nucleation of the $\varepsilon$-$Li_xV_2O_5$ phase in a previously unlithiated particle is energetically preferred over nucleation of the highly incommensurate $\gamma$-phase in the Li-rich particle. Such a sequence of phase transformations demonstrates an interplay between the thermodynamic transformation barrier and a barrier to interparticle transport. At the electrode scale, interparticle heterogeneities can

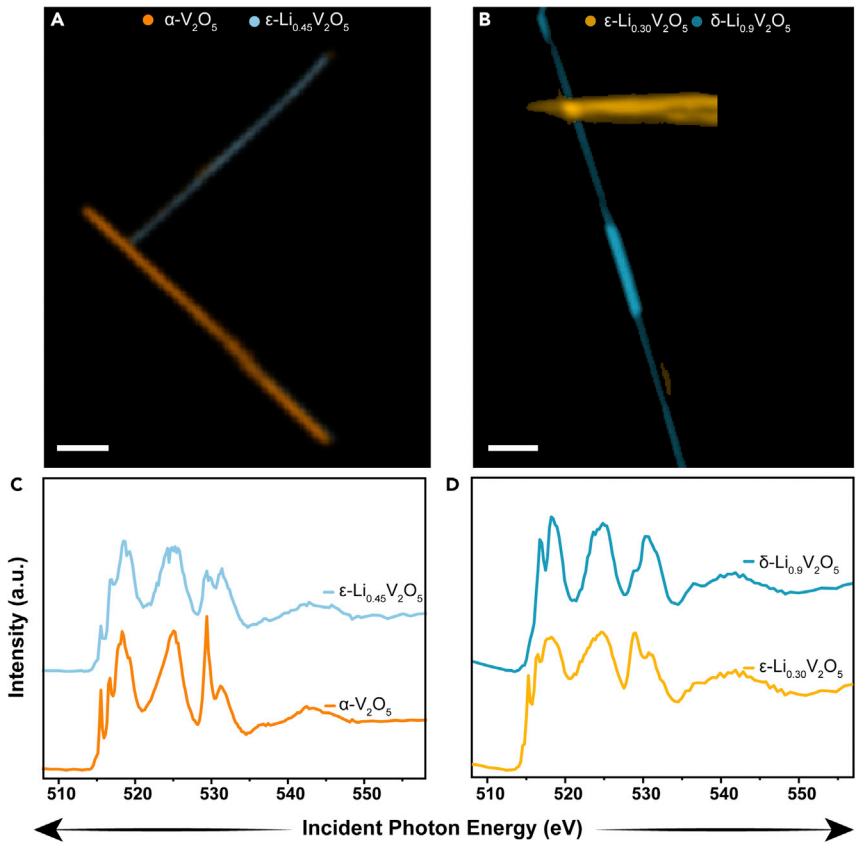


**Figure 5. Particle by particle lithiation at $V_2O_5$ particle interfaces**

(A–D) Nanowires lithiated by an "on-substrate" method exhibit particle-by-particle lithiation. Two sets of nanowires are shown in (A and B), wherein the colored regions in the composite maps correspond to the spectral components shown in (C and D), respectively, as identified by SVD with spectra from a combined principal-component and k-means clustering analysis informed by comparison with reference spectra. Orange (C)/yellow (D), and blue (C/D) regions demarcate locally low and highly lithiated wires and their corresponding spectral identity. Scale bars, 1 μm.

lead to significant variations in current density, driving high local current hotspots that can serve as a stress concentrator, nucleate crack formation, and accelerate degradation.[75] Approaches for mitigating interparticle differences include the formation of mesoscale architectures that maximize concurrent nucleation events[34] and modifying intercalation phase diagrams to stabilize extended solid-solution lithiation regimes.[76,77] As such, analysis of STXM composition and phase maps aided by reference spectra provide insight into the nature of interfaces between positive electrode particles, illustrating a preference for interparticle heterogeneity over intraparticle phase boundaries when particles are connected through interfaces that enable facile Li diffusion.[78] The heterogeneous transformation of individual particles drives a large fraction of the current to a small fraction of the active material, thereby contributing to local thermal and stress gradients.[24,79,80]

## Quantitative maps of mesoscale lithiation heterogeneities

At mesoscale dimensions, the spatiotemporal evolution of phase propagation fronts strongly depends on particle dimensions and geometry, their interfaces, (dis)charge rates, and their relative position in the electrode architecture.[16,23,26,30,72,81] An example of this is highlighted in Figure 6A, which shows the galvanostatic discharge/charge profiles of nanosphere (0D), nanowire (1D), nanoplatelet (2D), and micron-sized platelet bulk (3D) geometries (corresponding SEM images shown in Figures 6B–6E, respectively). Here, several voltage plateaus, corresponding to the individual phase transitions in the $V_2O_5$ phase diagram (Figure 6F), coincide with multiphase coexistence. Most notably, in this series, a size dependence on specific discharge capacity is observed, which reflects the higher internal resistance and diffusion limitations of larger particles. Not surprisingly, several efforts to mitigate transport limitations in positive electrode materials include a reduction in particle size. Nevertheless, a large fraction of commercial cathodes, prepared via slurry comprising the active material, binder, solvent, and other conductive additives, contain several geometric irregularities that can engender large heterogeneities. To this end, it is crucial to investigate how these irregularities are manifested across length scales from ensembles to entire porous electrodes.

Figures 6G–6L illustrate mesoscale lithiation heterogeneities in a representative ensemble of >83 polydisperse $Li_xV_2O_5$ nanoparticles, as illustrated by the scanning electron micrograph in Figure 6G. In previous work, a qualitative heuristic analysis of lithiation heterogeneities was performed on this dataset.[33] In the present work, accurate visualization of the spatial distribution of ε-$Li_{0.3}V_2O_5$ (Figure 6H), ε-$Li_{0.45}V_2O_5$ (Figure 6I), and δ-$Li_{0.9}V_2O_5$ (Figure 6J) is made possible by a comparison of clustered spectra (solid line, Figure 6K) against standards (dashed line, Figure 6K) to assess mesoscale lithiation heterogeneities quantitatively. At first glance, the phase maps shown in Figures 6H–6J point toward a size dependence of the extent of lithiation. Instance segmentation of each phase map by a deep learning model based on the Mask R-CNN algorithm[82] enables a quantitative assessment of this hypothesis by calculating the statistical distribution of particles represented by the ε-$Li_{0.3}V_2O_5$, ε-$Li_{0.45}V_2O_5$, and δ-$Li_{0.9}V_2O_5$ spectra (Figure S18). Figure 6L shows an inverse correlation between projected (2D) particle surface area and lithium stoichiometry, consistent with previous observations from modeling[83] and the cycling data shown in Figure 6A. Here, a reduction in particle size increases surface area (thereby increasing the interface between the active particle and the electrolyte/lithium source) and reduces diffusion pathlengths, which are particularly important in the case of orthorhombic $V_2O_5$, wherein significant changes in coordination environment engender ion-transport limitations.[33]

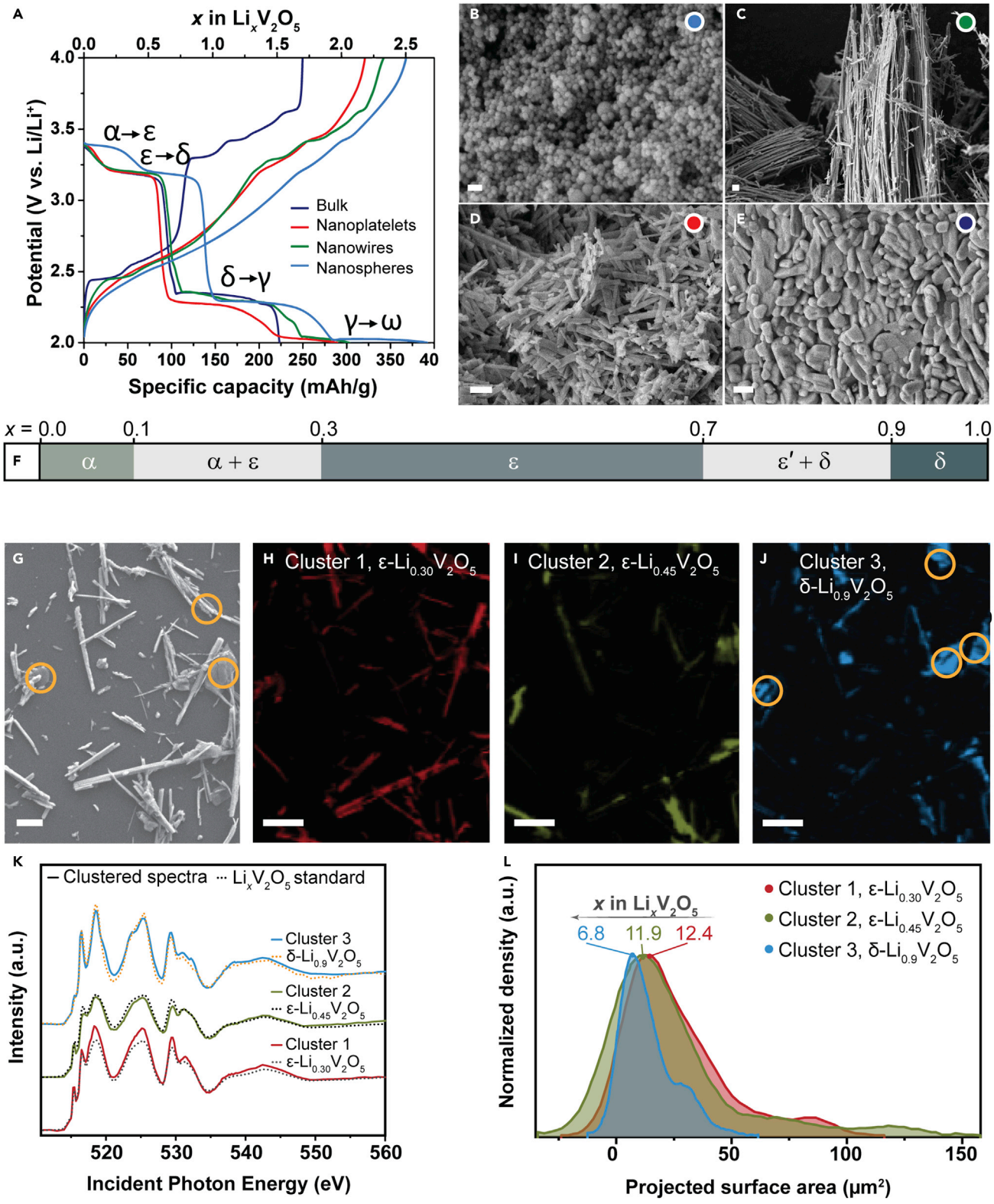


**Figure 6. Quantitative analysis of lithiation heterogeneities on an ensemble of $Li_xV_2O_5$ nanoparticles**

(A–E) (A) Discharge/charge profiles of various α-$V_2O_5$ particle geometries at a C-rate of C/5 for the first cycles between 2.0 and 4.0 V The morphology of the (B) nanospheres, (C) nanowires, (D) nanoplates, and (E) micron-sized "bulk" platelets is depicted by SEM Scale bars, 100 nm (B) and 1 μm (C–E), respectively. (F) A simplified phase diagram showing the evolution of lithiation-induced $Li_xV_2O_5$ phases is included in (F).

*(legend continued on next page)*

Notably, the mode values for the surface area of the closely lithiated ε-$Li_{0.3}V_2O_5$ (12.4 $\mu m^2$) and ε-$Li_{0.45}V_2O_5$ (11.9 $\mu m^2$) phases are in proximity, and in contrast to the formation of δ-$Li_{0.9}V_2O_5$, which is observed primarily in particles with a 6.8 $\mu m^2$ mode surface area. It should be noted here that the calculated surface area for smaller particles, in particular, is an overestimation due to feathering at particle edges, resulting from limited spatial resolution and the presence of agglomerations. Interestingly, a significant fraction of the larger particles in this distribution show regions that can best be represented by either ε-$Li_{0.3}V_2O_5$ or ε-$Li_{0.45}V_2O_5$, demonstrating compositional differences within individual particles (albeit within a single solid-solution regime) above a critical size threshold. This heterogeneity is likely driven at least in part by geometric asphericity[15] as well as the presence of extended defects within particles.[10,69] This quantitative view of phase coexistence and its size dependence provides a compelling illustration of the use of reference spectra acquired for well-defined standards. Through the lens of electrochemistry-mechanics coupling, scaling down particle dimensions increases the relative penalty associated with phase-boundary-induced interfacial mismatch, thus suppressing phase separation, an origin of stress and battery degradation.[83] Indeed, this quantitative mapping underscores the interplay between crystallite geometry and lithiation heterogeneities; whereas micrometer-sized platelets of $V_2O_5$ exhibit considerable phase heterogeneities across the thickness of the electrode; electrodes comprising homogenous-nanometer-sized spherical $V_2O_5$ show remarkably homogeneous lithiation with extended solid-solution lithiation.[16] Together, the results in Figure 6 attest to the importance of controlling electrochemistry-mechanics coupling to enhance electrode performance.

A closer investigation of the size distribution of the three phases in Figure 6 reveals that, following lithiation (discharge), a limited number of large and small particles remain lithiated (discharged) and delithiated (charged), respectively, reflecting a minority population that shows deviations from the norm. Indeed, this suggests that particle size is not the sole determinant of the sequence of intercalation events. As shown in Figures 4 and 5, for example, the presence of defects and interparticle connectivity can significantly alter phase separation patterns. In view of this, local considerations of electrode materials, proximity and accessibility of Li-ion exchange with adjacent particles, and geometric asphericity play a significant part in driving the observed intercalation phenomena.[15,30,34] This coupling between geometry, electrochemistry, and mechanics remains inadequately understood. However, it is clearly critical to realizing the full potential of intercalation electrodes,[84] such as $V_2O_5$, as demonstrated by recent studies leveraging geometry,[16,34] strain,[24,85–87] and atomistic modifications[35,88] as levers to modulate intercalation phase diagrams to circumvent significant phase inhomogeneities and stress gradients. Pint and coworkers demonstrated that straining $V_2O_5$ thin films through coupling with shape-memory alloys modulated intercalation potentials by as much as 40 mV and provided a 2.5× increase of the Li-ion diffusion coefficient.[85,86] Electrochemistry-mechanics coupling in cathode materials is a multiphysics problem that occurs over decades of length scales from atomic to mesoscale dimensions; visualizing these interactions through hyperspectral imaging, as shown in this work, is a step toward deciphering design principles for mitigating the consequences of battery degradation.

## Conclusions

The fundamental mechanisms of chemistry-geometry-mechanics coupling in Li-ion batteries remain inadequately understood but continue to be of pivotal importance to the lifetime of commercial batteries. Atomistic phenomena propagate across mesoscale dimensions, manifesting as phase inhomogeneities and stress gradients, which strongly impact the performance and longevity of electrode architectures. This work demonstrates the remarkable utility of synchrotron-based hyperspectral X-ray spectromicroscopy experiments, which, when coupled with spectral standards, enable accurate and quantitative mapping of inter- and intraparticle compositional heterogeneities, phase separation, and stress gradients in the canonical positive electrode material, α-$V_2O_5$. A detailed account of Li-intercalation-induced changes in the crystal lattice and electronic structure is developed to curate a robust set of physically interpretable spectral standards. Distinctive workflows, including SVD, PCA, k-means clustering, and linear combination fitting, are deployed in conjunction with reference spectra to develop high-accuracy quantitative maps.

Soft X-ray ptychography, informed by standards, enables high-resolution visualization of lithiation gradients, illuminating the role of defects and substrate coupling during nucleation-limited lithiation. Experimentally determined phase and composition maps at the level of individual particles are translated to stress gradients, enabling a direct link between chemistry and mechanics and providing key insights into the role of particle geometry in stress concentration. STXM imaging of interconnected particles reveals the delicate balance between barriers for phase nucleation, the energetic penalties associated with stabilizing phase boundaries, and Li-ion transport across interlinked particles. Finally, quantitative analysis of phase separation across an ensemble of nanoparticles demonstrates the role of particle size and geometry in governing phase separation and phase evolution. Deterministically controlling the trajectories of intercalation reactions remains a grand challenge for battery diagnostics and prognostics. Future efforts will focus on combining the chemical and spatial resolution of hyperspectral imaging with

(G) Scanning electron micrograph of >83 polydisperse $Li_xV_2O_5$ nanoparticles Scale bar, 2 μm
(H–J) Weighted maps obtained by SVD of the spectromicroscopy data (80 nm spatial resolution) using clustered spectra are shown for cluster 1 (H), cluster 2 (I), and cluster 3 (J). Scale bars, 2 μm (H–I). Thin nanosheets, outlined in yellow in (G and J) become highly lithiated due to the <100 nm dimensions along the plane-of-view are not considered during segmentation due to their departure from the nanowire morphology.
(K and L) Phase assignment of the clustered spectra (solid line) was determined by comparison with standards (dashed line) as shown in (K). A quantitative correlation between projected particle area and the extent of lithiation is provided in (L) based on the segmentation of the particles represented by each phase map.

temporal resolution within *operando* cells to track intercalation phenomena under an electrochemical stimulus with an eye toward developing design principles for real-time process control of key processes. In addition to the challenges of extracting correlators from dynamic imaging data, it is key to map laboratory measurements and the phenomenology observed in imaging experiments to data steams available in real-world applications. The latter are predominantly electrochemical impedance and current-voltage inputs monitored in battery management systems (BMSs). It is thus imperative to establish rigorously validated correlations and transfer functions between information-rich hyperspectral imaging data and impedance signals.[89,90] Such a capability could have tremendous potential for integrating meaningful performance descriptors into existing BMSs to monitor battery state-of-health and prolong battery service life.

## EXPERIMENTAL PROCEDURES

### Resource availability

#### *Lead contact*

Further information and requests for resources should be directed to and will be fulfilled by the lead contact, Sarbajit Banerjee (banerjee@chem.tamu.edu).

#### *Materials availability*

This study did not generate new materials.

#### *Data and code availability*

- The hyperspectral datasets, PXRD diffraction data, and X-ray absorption spectroscopy reference database can be found in a Mendeley Data repository: Santos, David (2022),"Multivariate Hyperspectral Data Analytics Across Length Scales to Probe Compositional, Phase, and Strain Heterogeneities in Electrode Materials," Mendeley Data, V1, https://doi.org/10.17632/797f2kfgbp.1.
- The original code used for generating composition maps and stress maps (via FEA) from hyperspectral imaging is included in the Mendeley Data repository.
- Access to the Analysis of X-ray Images and Spectra (aXis 2000) software is provided, free of charge, by Adam Hitchcock: http://unicorn.chemistry.mcmaster.ca/axis/aXis2000-download.html.
- Any additional information required to reanalyze the data reported in this paper is available from the lead contact upon request.

### Synthesis of various $V_2O_5$ particle morphologies

$\alpha$-$V_2O_5$ nanowires were synthesized by a hydrothermal growth process adapted from a previously reported method and range from 50 to 400 nm in width and thickness, respectively, and span several microns in length—the <400 nm thickness of the nanowires, parallel to the direction of the beam, ensure sample thickness is within the detector linearity region during STXM measurements.[24,34,41] In a typical reaction, 300 mg of commercially sourced $V_2O_5$ (Sigma Aldrich, 99.5%) was treated hydrothermally under reducing conditions (7:2 [v/v] mixture of water and 2-propanol; typically, the total reaction volume is 16 mL) to obtain green/blue $V_3O_7 \cdot H_2O$ nanowires. $V_2O_5$ nanowires were obtained by calcination of the recovered $V_3O_7 \cdot H_2O$ nanowires in static air at 350°C for 48 h.

The micron-sized platelet bulk (3D) geometries, shown in Figure 6E, were obtained from Alfa Aesar. $\alpha$-$V_2O_5$ nanospheres (Figure 6B) were synthesized based on a procedure outlined in previous work.[16] For the preparation of the nanoplatelet morphology (Figure 6D), 10 mL $H_2O_2$ (35 wt %) was slowly added into 0.36 g of bulk $V_2O_5$ (Alfa Aesar) with magnetic stirring and reacted for 10 min, followed by addition of 30 mL nano-pure water. The suspension was stirred continuously for 10 min. Next, 30 mL isopropanol was added, stirring the solution for another 10 min. The brown suspension was collected, transferred into a Teflon autoclave, and secured into a stainless-steel reactor. The reactor was placed into an oven and maintained at 180°C for 24 h. After cooling to room temperature (24 h), a precipitate was obtained through vacuum filtration. The precipitate was washed with nano-pure water and isopropanol and subquality dried under ambient conditions. Finally, the powder was annealed at 300°C for 24 h in the muffle furnace. For all morphologies, phase purity of the resulting orthorhombic $V_2O_5$ (*Pmmn*) was established by PXRD.

### Synthesis of stoichiometric $Li_xV_2O_5$ phases

$V_2O_5$ nanowires (300 mg) were initially dispersed in 20 mL of dry acetonitrile under an inert Ar atmosphere. A 1.25 M excess of the desired stoichiometric amount of anhydrous LiI (i.e., 0.1, 0.3, 0.45, 0.7, and 0.9 mol of LiI per mol of $V_2O_5$) was added to the acetonitrile/$V_2O_5$ mixture, which was allowed to stir gently for 7 days. Over the course of the reaction, the supernatant developed a brown/red color indicative of $I_2$ byproduct formation as per:

$$V_2O_5(s) + xLiI(MeCN) \leftrightarrow Li_xV_2O_5(s) + \frac{x}{2}I_2(MeCN). \quad \text{(Equation 3)}$$

Notably, $I_2$ acts as a mild oxidant and is sufficiently oxidizing so as to act as a chemical deintercalation agent. Consequently, reaction 2 is best characterized as reversible, and phase purity of the powder can be achieved at equilibrium. The stabilization of phase-pure $Li_xV_2O_5$ nanowires is key to construction and curation of a spectral database for well-characterized materials (Figures S6 and S7). This is in direct contrast to the use of the more highly reducing *n*-butyllithium (*vide infra*) as a lithiating agent, which is not reversible. The resulting $Li_xV_2O_5$ powders were separated from the supernatant by centrifugation and washed three times with dry acetonitrile to remove $I_2$ and excess unreacted LiI. After drying under an inert Ar atmosphere, phase purity was confirmed by PXRD (Figure 1A). X-ray absorption spectra obtained for each phase were collected in transmission mode (STXM) across V L- and O K-edges, as shown in Figures 1 and S4.

### PXRD

PXRD patterns were collected on a Bruker D8-focus diffractometer in Brag-Brentano geometry (Cu K$\alpha$, $\lambda$ = 1.5418 Å; 40 kV voltage; 25 mA current). Rietveld refinement of the X-ray diffraction patterns was performed using GSAS-II.[91]

### Chemical lithiation of $V_2O_5$ nanowires via *n*-butyllithium

Chemical lithiation of all samples not used as X-ray standards was achieved via immersion in a solution (molar excess of >4:1 Li:$V_2O_5$) of 0.025 M *n*-butyllithium (Sigma, Aldrich) in *n*-heptane under an inert atmosphere (Argon, <0.1 ppm $O_2$ and <0.1 ppm $H_2O$). Lithiation of the $V_2O_5$ nanowires proceeded according to:

$$V_2O_5(s) + xC_4H_9Li(C_7H_{16}) \rightarrow Li_xV_2O_5(s) + \frac{x}{2}C_8H_{18}(l). \quad \text{(Equation 4)}$$

The samples shown in Figures 4, 5A, 5B, and 6 were lithiated for 5, 5, 30, and 5 min, respectively. Relatively short lithiation times are employed to prevent saturation (i.e., complete lithiation) and to further reflect the early stages of lithiation (low depth of discharge). In contrast, longer lithiation times reflect a deeper depth of discharge.

The particles shown in Figure 6 were lithiated as a powder, utilizing a previously detailed procedure.[41] Here, the lithiated $V_2O_5$ powders were dispersed via ultrasonication in a 2-propanol (5 mg/mL) solution and subsequently drop cast onto a silicon nitride substrate.

The nanoparticles shown in Figures 4 and 5 were drop cast prior to lithiation.[24,34] An on-substrate lithiation protocol allows for the effects of interconnectivity on lithiation to be probed. For all samples, the as-prepared grids were immediately sealed under an inert argon atmosphere for transport to the Canadian Light Source and the Advanced Light Source for STXM and ptychography measurements, respectively.

### Galvanostatic measurements

Galvanostatic measurements were carried out using coin cells (CR2032) assembled in a glove box filled with argon gas. The working electrode was prepared by casting a mixture of active material ($V_2O_5$ powder), conductive carbon black (Super C45, MTI Corp.), and binder (poly(vinylidene fluoride)), with a weight ratio of 70:20:10 (w/w/w) in N-methyl-2-pyrrolidinone solution onto an aluminum foil as a current collector. A lithium foil (Sigma-Aldrich)

was utilized as the reference electrode. A Celgard 2500 membrane and a 1 M solution of $LiPF_6$ in ethylene carbonate and dimethyl carbonate (Sigma Aldrich) were used as the separator and electrolyte, respectively. Galvanostatic discharge-charge measurements of the coin cells were performed on a Land (CT2001A) system under a voltage window between 2.0 and 4.0 V at 25°C.

### STXM

The STXM measurements in Figures 5 and 6 were performed at the 10ID-1 beamline of the Canadian Light Source in Saskatoon, SK, CA. The 10ID-1 beamline is equipped with an elliptically polarized Apple II type undulator, which provides an intense beam in the 130–2,700 eV energy range. State-of-the-art Fresnel zone plate optics are utilized in conjunction with an order-sorting aperture to achieve a focused X-ray beam. The regions of interest shown in Figures 4A, 5A, 5B, and 6 were imaged with a spatial resolution of 50, 30, 50, and 80 nm, respectively. Regions of interest were defined based on experimental goals, i.e., the study of single particles, interconnected particles, or particle ensembles. Typically, ROIs are located using single-energy X-ray microscopy measurements. Before spectromicroscopy experiments, an average composition is estimated from a line-scan (ensemble X-ray spectroscopy). For the STXM measurements shown in Figures 4, 5, and 6, the V L- and the O K-edges were collected in a single stack ranging from 508 to 560 eV with energy steps of 0.2 eV in the regions of spectral interest (Figure 1) and 1 eV in the continuum regions before and after the specific elemental edges. In a typical STXM measurement, a region of interest is raster-scanned while transmission intensities are recorded in a stepwise fashion by a charged-couple device detector. A 500-line $mm^{-1}$ monochromator was used to tune the incident photon energy to the V L- and O K-edges for imaging the $Li_xV_2O_5$ samples; here, a 1 ms $pixel^{-1}$ $energy^{-1}$ dwell time was used for signal acquisition.

Image registration was achieved by a cross-correlation analysis using the "Jacobsen stack analyze" routine in the aXis2000 software suite (version updated May 28, 2022). An incident spectrum was collected from a fully transmitting region in the sample (i.e., the silicon nitride substrate) to convert the transmission measurements to an optical density matrix. Preliminary screenings of the data were recorded by integrating the spectra across all pixels to obtain an averaged spectrum that could be compared indirectly or directly to energy-calibrated reference spectra. Spectral shape, peak positions, and relative peak intensities are qualitatively assessed in an indirect comparison, whereas a direct comparison fits a linear combination of the standard spectra to experimental spectra in the Athena suite offered by the Demeter software package (http://bruceravel.github.io/demeter/).

PCA and subsequent k-means clustering were carried out using the "PCA_GUI" routine (version 1.1.1) within aXis2000. The number of principal components considered for clustering was chosen based on their eigenvalues and their corresponding eigenspectrum/eigenimage representation of the data. Access to the analytical standards aids in a preliminary interpretation of the eigenspectra, which considerably improves the selection of significant components. The number of clusters sought by a subsequent k-means search was refined by comparison with standards and by linear combination fitting of experimental spectra with standards. The averaged spectrum for each cluster was then assigned a lithium stoichiometry of $x = 0$, $x = 0.1$, $x = 0.3$, $x = 0.45$, or $x = 0.7$ in $Li_xV_2O_5$ to obtain a set of phase-specific signatures from which composition maps could be generated by SVD (*vide infra*).

### X-ray ptychography

The X-ray ptychography measurements shown in Figure 4 were performed at the coherent scattering and microscopy beamline (COSMIC) 7.0.1.2 of the Advanced Light Source in Berkeley, CA. The recursive translation function of the StackReg plugin within ImageJ (https://imagej.nih.gov/ij/) was utilized to register ptychography images generated in a stepwise fashion along the V L-edge. The particles in Figure 4 were initially imaged by STXM with a spatial resolution of 50 nm, and an energy resolution of 0.2 eV in the regions of spectral interest (Figure 1) and 1 eV in the continuum regions before and after the specific elemental edges—their averaged spectra were compared against standards to fingerprint $Li_xV_2O_5$ phases. Single-energy X-ray pytchyogrpahy images were collected with 10 nm spatial resolution at energies corresponding to the $d_{xy}$, $d_{xz/yz}$, and post-edge features (energy positions were directly informed by the averaged spectrum from STXM). Relative intensities at the $d_{xy}$ and $d_{xz/yz}$ were assessed to infer lithiation gradients after normalizing for thickness effects based on pixel intensities at the post-edge.

### Construction of a test STXM dataset

A synthetic stack can be generated (as opposed to experimentally collected) from a single image (Figure S19A) and spectrum (Figure S19B) in the aXis2000 software suite. In brief, for a given spectrum with $N$ number of absorption measurements (determined by the incident photon energy range and step size [eV]), the resulting stack comprises $N$ images containing pixel values that result from the product of the pixel intensity in the original image and the energy-specific absorption intensity as shown in Figure S19C.

Intraparticle heterogeneity was simulated by creating a synthetic stack dataset comprising three spectroscopically distinct regions. The images in Figures S8A and S8C were combined with the reference spectra (Figure 1F) in Figures S8D and S8F, which represent phase-pure $\alpha$-$Li_{0.1}V_2O_5$ and $\varepsilon$-$Li_{0.45}V_2O_5$, respectively. Figures S8B and S8E correspond to a phase mixture comprised of 70% $\varepsilon$-$Li_{0.45}V_2O_5$ and 30% $\alpha$-$Li_{0.1}V_2O_5$ (generated from a weighted average of the spectra in Figures S8D and S8F). The importance of accounting for regions with intermediate concentration (within the spinodal region) is 2-fold; first, thin metastable interfaces between Li-rich and Li-poor domains have been experimentally observed,[24] and, second, phase boundaries oriented along the direction of the incident X-rays are possible based on the orientation of the nanowire to the substrate as shown in Figure S20.

### Generation of composition maps from STXM data

Prior to performing SVD, spectra obtained directly from standards or a standards-informed PCA selection and k-means analyses were converted to a mass absorption scale by matching the pre- and post-edge absorption intensities to the sum of the tabulated atomic mass attenuation coefficients for each material composition and density to enable quantitative analysis. The results of applying SVD to STXM data include a set of phase maps that describe the spectral weighting of each component and thickness in every pixel, as shown in Figure S9. In this work, the generation of high-resolution composition maps has been adapted from a previously reported procedure that directly uses the spectral maps to visualize composition.[24,34,53]

To reduce noise and enable a continuous representation of the data, the spectral maps generated from the SVD process were subjected to a Gaussian filter $G$, according to:

$$G(x,y) = \frac{1}{2\pi\sigma} e^{-\left(\frac{x^2+y^2}{2\sigma^2}\right)}, \qquad \text{(Equation 5)}$$

where $\sigma$ denotes the filter width—increasing the value of $\sigma$ leads to a broader "smearing" of the input data over the image plane. This work uses the multidimensional Gaussian filter from the SciPy package for smoothing.[92] The $\sigma$ hyperparameter of the Gaussian filter is chosen based on the spectral resolution of the original image ($\sigma = 1$, mode = "reflect"). The remaining default settings were retained from the SciPy package. A bilinear interpolation enables a continuous representation of the data to better visualize the spatial orientation of distinctly lithiated domains. This work uses Omni's calculator (https://www.omnicalculator.com/math/bilinear-interpolation) to perform bilinear interpolation on each spectral map. Subsequently, the superposition of the pixel intensities contained in the spectral maps are weighted by the corresponding stoichiometric fraction $x_i$ for each spectral map (informed by standards), yields a composition map according as:

$$C(x,y) = \sum \tilde{\varphi}_i(x,y)\, x_i, \qquad \text{(Equation 6)}$$

where $\tilde{\varphi}_i$ denotes the intensity value at a given pixel after Gaussian transformation, and $i$ denotes the number of phases in $Li_xV_2O_5$. The composition $C$ at each pixel is thus derived from a superposition of the various lithiated phases present in each pixel, as inferred from a standards-informed deconvolution of the phase mixtures. To avoid the introduction of errors during bilinear interpolation, composition maps have been contrasted before and after the interpolation step—no notable inconsistencies were identified.

To calculate stress maps, a finite element mesh is first generated from the composition map using the open-source mesh generator GMSH. The *find_contour* function within the scikit-image library applies the marching square algorithm to extract the particle's geometry, which aids in mesh generation. Subsequently, local lithium stoichiometries are mapped onto the nodes of the planar triangle mesh utilizing a linear interpolation according to:

$$c = c_{min} + (x - x_{min})\left(\frac{c_{max} - c_{min}}{x_{max} - x_{min}}\right), \quad \text{(Equation 7)}$$

where $c_{min}$ and $c_{max}$ denote the lower and upper bounds of the lithium concentration at corresponding composition bounds $x_{min}$ *and* $x_{max}$ according to literature data (Table S14).

For a general case, nonlinear kinematics and inelasticity are expected. Linear elasticity is assumed wherein a constitutive relationship links stresses and strains according to:

$$\sigma_{ij} = C_{ijkl}\varepsilon^{el}_{kl}, \quad \text{(Equation 8)}$$

with a fourth-order elasticity tensor, $C_{ijkl}$, that describes the linear dependence between the symmetric second-order stress tensor $\sigma_{ij}$ on the elastic strain $\varepsilon^{el}_{kl}$, which can be further defined according to:

$$\varepsilon^{el}_{kl} = \varepsilon_{kl} - c\Omega_{kl}, \quad \text{(Equation 9)}$$

where $\varepsilon_{kl}$ denotes the second-order infinitesimal strain tensor, $\Omega_{kl}$ is the strain change related to lithiated $V_2O_5$ (values from a linear interpolation of unit cell parameters are shown in Table S14). In the special case of isotropic volume change, $\Omega_{kl} = \frac{1}{3}\Omega\delta_{kl}$, with $\Omega$ being the partial molar volume change and $\delta_{kl}$ the unit tensor with components *k* and *l*. In the finite element simulations, lithiation-induced deformations of the $Li_xV_2O_5$ intercalation host are described by the linearized strain tensor defined as:

$$\varepsilon_{ij} = \frac{1}{2}(u_{i,j} + u_{j,i}), \quad \text{(Equation 10)}$$

where $u_i$ denotes the components of the displacement vector. To visualize the resulting stress states and their proximity to failure in the present material system, the von Mises stress is calculated as

$$\sigma_v = \sqrt{\sigma_x^2 + \sigma_y^2 - \sigma_x\sigma_y + 3\tau_{xy}^2}, \quad \text{(Equation 11)}$$

where the equivalent von Mises stress $\sigma_v$, and $\sigma_x$, $\sigma_y$, and $\tau_{xy}$, denote the normal and shear stress components in Cartesian coordinates (see supplemental information and Figures S21–S23). For simplicity, isotropic material behavior and a concentration-independent Young's modulus of $E$ = 43 GPa, Poisson's ratio of $\nu$ = 0.3 were assumed for the finite element simulations.[24,49] Both fixed and free boundary conditions were considered to account for the constrained and unconstrained volumetric expansion of the particle boundaries, resulting from varying degrees of particle-particle or particle-substrate surface interactions. The fully constrained and unconstrained conditions examined here enable a quantitative estimation of the upper and lower bound of von Mises stress developed within single particles. The overall stress level for the constrained conditions is nearly 2- to 3-fold greater when compared with the unconstrained alternative. Constraining the boundaries affects a stress state shift toward the compressive regime, an overall increase in the magnitude of stresses, and $\tau_{\xi\eta}$ "hotspots" at phase interfaces, as shown in Figures S13 and S18.

## SUPPLEMENTAL INFORMATION

Supplemental information can be found online at https://doi.org/10.1016/j.patter.2022.100634.

## ACKNOWLEDGMENTS

We acknowledge support from the National Science Foundation (NSF) Award CMMI-2038625 as part of the NSF/DHS/DOT/NIH/USDA-NIFA Cyber-Physical Systems Program. Spectral data collection, database curation, and spectral signature assignment was funded by the NSF under Award DMR 1627197. The research was funded in part by award A-1978-20190330 from the Welch Foundation. A portion of the research described in this article was performed at the Canadian Light Source (SM beamline), which is supported by the Natural Sciences and Engineering Research Council of Canada, the National Research Council Canada, the Canadian Institutes of Health Research, the Province of Saskatchewan, Western Economic Diversification Canada, and the University of Saskatchewan. We thank Dr. Jian Wang at beamline 10ID1 of the Canadian Light Source for support and for STXM data collection. The authors further acknowledge the Advanced Light Source (ALS) and Dr. David Shapiro for assistance with X-ray ptychography data collection. D.A.S. acknowledges support from an NSF Graduate Research Fellowship under grant no. 1746932. B.L. and B.-X.X. acknowledge the financial support from the Federal Ministry of Education and Research (BMBF) and the state of Hesse as part of the NHR Program, as well as support under grant agreement no. 405422877 of the Paper Research project (FiPRe). B.L. and B.-X.X. also gratefully acknowledge the computing time granted by the NHR4CES Resource Allocation Board and provided on the supercomputer Lichtenberg II at TU Darmstadt as part of the NHR4CES infrastructure. The stress and composition calculations for this research were conducted with computing resources under the project project1020, special0007.

## AUTHOR CONTRIBUTIONS

D.A.S., conceptualization, formal analysis, investigation, data curation, methodology, writing – original draft, visualization. J.L.A., conceptualization, formal analysis, investigation, data curation, visualization, writing – original draft. B.L., formal analysis, methodology, visualization, writing – original draft. L.R.D.J., conceptualization, investigation. Y.L., investigation, formal analysis. S.P., formal analysis. M.A.G., investigation. L.C., investigation. P.S., methodology. Y.D., supervision. B.-X.X., supervision, funding acquisition. S.B., supervision, funding acquisition, writing – review & editing.

## DECLARATION OF INTERESTS

The authors declare no competing interests.

## INCLUSION AND DIVERSITY

One or more of the authors of this paper self-identifies as an underrepresented ethnic minority in their field of research or within their geographical location. One or more of the authors of this paper self-identifies as a gender minority in their field of research. One or more of the authors of this paper self-identifies as a member of the LGBTQIA+ community. One or more of the authors of this paper received support from a program designed to increase minority representation in their field of research. While citing references scientifically relevant for this work, we also actively worked to promote gender balance in our reference list.

Received: June 24, 2022
Revised: August 2, 2022
Accepted: October 21, 2022
Published: November 17, 2022

## REFERENCES

1. Whittingham, M.S. (2020). Lithium batteries: 50 years of advances to address the next 20 Years of climate issues. Nano Lett. *20*, 8435–8437. https://doi.org/10.1021/acs.nanolett.0c04347.
2. Cano, Z.P., Banham, D., Ye, S., Hintennach, A., Lu, J., Fowler, M., Chen, Z., Cano, Z.P., Banham, D., Ye, S., et al. (2018). Batteries and fuel cells for emerging electric vehicle markets. NatEn *3*, 279. https://www.nature.com/articles/s41560-018-0108-1.
3. Kim, T., Song, W., Son, D.-Y., Ono, L.K., and Qi, Y. (2019). Lithium-ion batteries: outlook on present, future, and hybridized technologies. J. Mater. Chem. A Mater. *7*, 2942–2964. https://doi.org/10.1039/C8TA10513H.
4. Xing, F., Bi, Z., Su, F., Liu, F., Wu, Z.-S., Xing, F., Bi, Z., Su, F., Liu, F., and Wu, Z.-S. (2022). Unraveling the design principles of battery-supercapacitor

hybrid devices: from fundamental mechanisms to microstructure engineering and challenging perspectives. Adv. Energy Mater. 2200594. https://doi.org/10.1002/aenm.202200594.

5. Lewis, J.A., Tippens, J., Cortes, F.J.Q., and McDowell, M.T. (2019). Chemo-mechanical challenges in solid-state batteries. Trends Chem. *1*, 845–857. https://doi.org/10.1016/j.trechm.2019.06.013.

6. Zhao, K., and Cui, Y. (2016). Understanding the role of mechanics in energy materials: a perspective. Extreme Mech. Lett. *9*, 347–352. https://doi.org/10.1016/j.eml.2016.10.003.

7. Waldmann, T., Iturrondobeitia, A., Kasper, M., Ghanbari, N., Aguesse, F., Bekaert, E., Daniel, L., Genies, S., Gordon, I.J., Löble, M.W., et al. (2016). Review—post-mortem analysis of aged lithium-ion batteries: disassembly methodology and physico-chemical analysis techniques. J. Electrochem. Soc. *163*, A2149–A2164. https://doi.org/10.1149/2.1211609jes.

8. Li, W., Lutz, D.M., Wang, L., Takeuchi, K.J., Marschilok, A.C., and Takeuchi, E.S. (2021). Peering into batteries: electrochemical insight through in situ and operando methods over multiple length scales. Joule *5*, 77–88. https://doi.org/10.1016/j.joule.2020.11.003.

9. Edge, J.S., O'Kane, S., Prosser, R., Kirkaldy, N.D., Patel, A.N., Hales, A., Ghosh, A., Ai, W., Chen, J., Yang, J., et al. (2021). Lithium ion battery degradation: what you need to know. Phys. Chem. Chem. Phys. *23*, 8200–8221. https://doi.org/10.1039/D1CP00359C.

10. Bai, Y., Santos, D.A., Rezaei, S., Stein, P., Banerjee, S., and Xu, B.-X. (2021). A chemo-mechanical damage model at large deformation: numerical and experimental studies on polycrystalline energy materials. Int. J. Solids Struct. *228*, 111099. https://doi.org/10.1016/j.joule.2020.11.003.

11. Zhang, Y., Yang, Z., and Tian, C. (2019). Probing and quantifying cathode charge heterogeneity in Li ion batteries. J. Mater. Chem. A Mater. *7*, 23628–23661. https://doi.org/10.1039/C9TA06977A.

12. Zhao, Y., Stein, P., Bai, Y., Al-Siraj, M., Yang, Y., and Xu, B.X. (2019). A review on modeling of electro-chemo-mechanics in lithium-ion batteries. J. Power Sources *413*, 259–283. https://doi.org/10.1016/j.jpowsour.2018.12.011.

13. Cogswell, D.A., and Bazant, M.Z. (2012). Coherency strain and the kinetics of phase separation in LiFePO4 nanoparticles. ACS Nano *6*, 2215–2225. https://doi.org/10.1021/nn204177u.

14. Tsao, J.Y. (1993). Coherency and semi-coherency. In Materials Fundamentals of Molecular Beam Epitaxy (Elsevier), pp. 151–197. https://doi.org/10.1016/B978-0-08-057135-5.50013-4.

15. Mistry, A., Heenan, T., Smith, K., Shearing, P., and Mukherjee, P.P. (2022). Asphericity can cause nonuniform lithium intercalation in battery active particles. ACS Energy Lett. *7*, 1871–1879. https://doi.org/10.1021/acsenergylett.2c00870.

16. Luo, Y., Bai, Y., Mistry, A., Zhang, Y., Zhao, D., Sarkar, S., Handy, J.v., Rezaei, S., Chuang, A.C., Carrillo, L., et al. (2022). Effect of crystallite geometries on electrochemical performance of porous intercalation electrodes by multiscale operando investigation. Nat. Mater. *21*, 217–227. https://doi.org/10.1038/s41563-021-01151-8.

17. Yang, K., and Tang, M. (2020). Three-dimensional phase evolution and stress-induced non-uniform Li intercalation behavior in lithium iron phosphate. J. Mater. Chem. A Mater. *8*, 3060–3070. https://doi.org/10.1039/C9TA11697D.

18. Wolf, M., May, B.M., and Cabana, J. (2017). Visualization of electrochemical reactions in battery materials with X-ray microscopy and mapping. Chem. Mater. *29*, 3347–3362. https://doi.org/10.1021/acs.chemmater.6b05114.

19. Merryweather, A.J., Schnedermann, C., Jacquet, Q., Grey, C.P., and Rao, A. (2021). Operando optical tracking of single-particle ion dynamics in batteries. Nature *594*, 522–528. https://doi.org/10.1038/s41586-021-03584-2.

20. Yuan, Y., Amine, K., Lu, J., and Shahbazian-Yassar, R. (2017). Understanding materials challenges for rechargeable ion batteries with in situ transmission electron microscopy. Nat. Commun. *8*, 1–14. https://doi.org/10.1038/ncomms15806.

21. Quinn, A., Moutinho, H., Usseglio-Viretta, F., Verma, A., Smith, K., Keyser, M., and Finegan, D.P. (2020). Electron backscatter diffraction for investigating lithium-ion electrode particle architectures. Cell Rep. Phys. Sci. *1*, 100137. https://doi.org/10.1016/j.xcrp.2020.100137.

22. Gong, Y., Chen, Y., Zhang, Q., Meng, F., Shi, J.A., Liu, X., Liu, X., Zhang, J., Wang, H., Wang, J., et al. (2018). Three-dimensional atomic-scale observation of structural evolution of cathode material in a working all-solid-state battery. Nat. Commun. *9*, 1–8. https://doi.org/10.1038/s41467-018-05833-x.

23. Cogswell, D.A., and Bazant, M.Z. (2018). Size-dependent phase morphologies in LiFePO4 battery particles. Electrochem. Commun. *95*, 33–37. https://doi.org/10.1016/j.elecom.2018.08.015.

24. Santos, D.A., Andrews, J.L., Bai, Y., Stein, P., Luo, Y., Zhang, Y., Pharr, M., Xu, B.X., and Banerjee, S. (2020). Bending good beats breaking bad: phase separation patterns in individual cathode particles upon lithiation and delithiation. Mater. Horiz. *7*, 3275–3290. https://doi.org/10.1039/D0MH01240H.

25. Lim, J., Li, Y., Alsem, D.H., So, H., Lee, S.C., Bai, P., Cogswell, D.A., Liu, X., Jin, N., Yu, Y.S., et al. (2016). Origin and hysteresis of lithium compositional spatiodynamics within battery primary particles. Science *353*, 566–571. https://doi.org/10.1126/science.aaf4914.

26. Chueh, W.C., el Gabaly, F., Sugar, J.D., Bartelt, N.C., McDaniel, A.H., Fenton, K.R., Zavadil, K.R., Tyliszczak, T., Lai, W., and McCarty, K.F. (2013). Intercalation pathway in many-particle LiFePO4 electrode revealed by nanoscale state-of-charge mapping. Nano Lett. *13*, 866–872. https://doi.org/10.1021/nl3031899.

27. Urquhart, S.G. (2022). X-Ray spectroptychography. ACS Omega *7*, 11521–11529. https://doi.org/10.1021/acsomega.2c00228.

28. Du, M., and Jacobsen, C. (2018). Relative merits and limiting factors for x-ray and electron microscopy of thick, hydrated organic materials. Ultramicroscopy *184*, 293–309. https://doi.org/10.1016/j.ultramic.2017.10.003.

29. Hitchcock, A.P. (2015). Soft X-ray spectromicroscopy and ptychography. J. Electron Spectros. Relat. Phenomena *200*, 49–63. https://doi.org/10.1016/j.elspec.2015.05.013.

30. Li, J., Sharma, N., Jiang, Z., Yang, Y., Monaco, F., Xu, Z., Hou, D., Ratner, D., Pianetta, P., Cloetens, P., et al. (2022). Dynamics of particle network in composite battery cathodes. Science *376*, 517–521. https://doi.org/10.1126/science.abm8962.

31. Li, Y., Meyer, S., Lim, J., Chul Lee, S., Gent, W.E., Marchesini, S., Krishnan, H., Tyliszczak, T., Shapiro, D., David Kilcoyne, A.L., et al. (2015). Effects of particle size, electronic connectivity, and incoherent nanoscale domains on the sequence of lithiation in LiFePO4 porous electrodes. Adv. Mater. *27*, 6591–6597. https://doi.org/10.1002/adma.201502276.

32. Yao, J., Li, Y., Massé, R.C., Uchaker, E., and Cao, G. (2018). Revitalized interest in vanadium pentoxide as cathode material for lithium-ion batteries and beyond. Energy Storage Mater. *11*, 205–259. https://doi.org/10.1016/j.ensm.2017.10.014.

33. de Jesus, L.R., Andrews, J.L., Parija, A., and Banerjee, S. (2018). Defining diffusion pathways in intercalation cathode materials: some lessons from $V_2O_5$ on directing cation traffic. ACS Energy Lett. *3*, 915–931. https://doi.org/10.1021/acsenergylett.8b00156.

34. Andrews, J.L., Stein, P., Santos, D.A., Chalker, C.J., de Jesus, L.R., Davidson, R.D., Gross, M.A., Pharr, M., Batteas, J.D., Xu, B.X., et al. (2020). Curvature-induced modification of mechano-electrochemical coupling and nucleation kinetics in a cathode. Material. Matter *3*, 1754–1773. https://doi.org/10.1073/pnas.2115072119.

35. Luo, Y., Rezaei, S., Santos, D.A., Zhang, Y., Handy, J.v., Carrillo, L., Schultz, B.J., Gobbato, L., Pupucevski, M., Wiaderek, K., et al. (2022). Cation reordering instead of phase transitions: origins and implications of contrasting lithiation mechanisms in 1D $\zeta$- and 2D $\alpha$-$V_2O_5$. Proc. Natl. Acad. Sci. USA *119*. https://doi.org/10.1073/pnas.211507211.

36. Watthaisong, P., Jungthawan, S., Hirunsit, P., and Suthirakun, S. (2019). Transport properties of electron small polarons in a $V_2O_5$ cathode of

Li-ion batteries: a computational study. RSC Adv. *9*. 19483–19494. https://doi.org/10.1039/C9RA02923K.

37. Diem, A.M., Bill, J., and Burghard, Z. (2020). Creasing highly porous $V_2O_5$ scaffolds for high energy density aluminum-ion batteries. ACS Appl. Energy Mater. *3*, 4033–4042. https://doi.org/10.1021/acsaem.0c00455.
38. Santos, D.A., Dixit, M.K., Pradeep Kumar, P., and Banerjee, S. (2021). Assessing the role of vanadium technologies in decarbonizing hard-to-abate sectors and enabling the energy transition. iScience *24*, 103277. https://doi.org/10.1016/j.isci.2021.103277.
39. Brown, E., Park, S.-H., Elangovan, A., Yuan, Y., Kim, J., Sun, X.S., Zhang, X., Wang, G., and Li, J. (2018). Facilitating high-capacity $V_2O_5$ cathodes with stable two and three Li+ insertion using a hybrid membrane structure consisting of amorphous $V_2O_5$ shells coaxially deposited on electrospun carbon nanofibers. Electrochim. Acta *269*, 144–154. https://doi.org/10.1016/j.electacta.2018.02.167.
40. Zhou, Y.Y., Zhang, Z.Y., Zhang, H.Z., Li, Y., and Weng, Y. (2021). Progress and perspective of vanadium-based cathode materials for lithium ion batteries. Tungsten *3*, 279–288. https://doi.org/10.1007/s42864-021-00115-4.
41. Horrocks, G.A., Likely, M.F., Velazquez, J.M., and Banerjee, S. (2013). Finite size effects on the structural progression induced by lithiation of $V_2O_5$: a combined diffraction and Raman spectroscopy study. J. Mater. Chem. A Mater. *1*, 15265. https://doi.org/10.1039/C3TA13690F.
42. Shih, B.C., Xue, Y., Zhang, P., Cohen, M.L., and Louie, S.G. (2010). Quasiparticle band gap of ZnO: high accuracy from the conventional G0W0 approach. Phys. Rev. Lett. *105*, 146401. https://doi.org/10.1103/PhysRevLett.105.146401.
43. Lany, S. (2013). Band-structure calculations for the 3d transition metal oxides in GW. Phys. Rev. B Condens. Matter Mater. Phys. *87*, 085112. https://doi.org/10.1103/PhysRevB.87.085112.
44. Liang, Y., Vinson, J., Pemmaraju, S., Drisdell, W.S., Shirley, E.L., and Prendergast, D. (2017). Accurate X-ray spectral predictions: an advanced self-consistent-field approach inspired by many-body perturbation theory. Phys. Rev. Lett. *118*, 096402. https://doi.org/10.1103/PhysRevLett.118.096402.
45. Nesvizhskii, A.I., and Rehr, J.J. (1999). L-edge XANES of 3d-transition metals. J. Synchrotron Radiat. *6*, 315–316. https://doi.org/10.1107/S0909049599001697.
46. DeBeer George, S., Petrenko, T., and Neese, F. (2008). Prediction of iron K-edge absorption spectra using time-dependent density functional theory. J. Phys. Chem. A *112*, 12936–12943. https://doi.org/10.1021/jp803174m.
47. Maganas, D., Roemelt, M., Hävecker, M., Trunschke, A., Knop-Gericke, A., Schlögl, R., and Neese, F. (2013). First principles calculations of the structure and V L-edge X-ray absorption spectra of $V_2O_5$ using local pair natural orbital coupled cluster theory and spin–orbit coupled configuration interaction approaches. Phys. Chem. Chem. Phys. *15*, 7260–7276. https://doi.org/10.1039/C3CP50709B.
48. Goering, E., Müller, O., Klemm, M., denBoer, M.L., and Horn, S. (1997). Angle dependent soft-X-ray absorption spectroscopy of $V_2O_5$. Phil. Mag. B *75*, 229–236. https://doi.org/10.1080/13642819708202311.
49. de Jesus, L.R., Horrocks, G.A., Liang, Y., Parija, A., Jaye, C., Wangoh, L., Wang, J., Fischer, D.A., Piper, L.F.J., Prendergast, D., et al. (2016). Mapping polaronic states and lithiation gradients in individual $V_2O_5$ nanowires. Nat. Commun. *7*, 12022. https://doi.org/10.1038/ncomms12022.
50. Lerotic, M., Mak, R., Wirick, S., Meirer, F., and Jacobsen, C. (2014). MANTiS : a program for the analysis of X-ray spectromicroscopy data. J. Synchrotron Radiat. *21*, 1206–1212. https://doi.org/10.1107/S1600577514013964.
51. Lerotic, M., Jacobsen, C., Schäfer, T., and Vogt, S. (2004). Cluster analysis of soft X-ray spectromicroscopy data. Ultramicroscopy *100*, 35–57. https://doi.org/10.1016/j.ultramic.2004.01.008.
52. Koprinarov, I.N., Hitchcock, A.P., McCrory, C.T., and Childs, R.F. (2002). Quantitative mapping of structured polymeric systems using singular value decomposition analysis of soft X-ray images. J. Phys. Chem. B *106*, 5358–5364. https://doi.org/10.1021/jp013281l.
53. de Jesus, L.R., Stein, P., Andrews, J.L., Luo, Y., Xu, B.-X.X., and Banerjee, S. (2018). Striping modulations and strain gradients within individual particles of a cathode material upon lithiation. Mater. Horiz. *5*, 486–498. https://doi.org/10.1039/C8MH00037A.
54. Velazquez, J.M., Jaye, C., Fischer, D.A., and Banerjee, S. (2009). Near edge X-ray absorption fine structure spectroscopy studies of single-crystalline V 2O 5 nanowire arrays. J. Phys. Chem. C *113*, 7639–7645. https://doi.org/10.1021/jp900809y.
55. Collins, B.A., and Ade, H. (2012). Quantitative compositional analysis of organic thin films using transmission NEXAFS spectroscopy in an X-ray microscope. J. Electron Spectros. Relat. Phenomena *185*, 119–128. https://doi.org/10.1016/j.elspec.2012.05.002.
56. Razifar, P., Muhammed, H.H., Engbrant, F., Svensson, P.-E., Olsson, J., Bengtsson, E., Långström, B., and Bergström, M. (2009). Performance of principal component analysis and independent component analysis with respect to signal extraction from noisy positron emission tomography data - a study on computer simulated images. Open Neuroimag. J. *3*, 1. https://doi.org/10.2174/1874440000903010001.
57. Ding, C., and He, X. (2004). *K* -means clustering via principal component analysis. In Twenty-first international conference on Machine learning - ICML '04 (ACM Press), p. 29. https://doi.org/10.1145/1015330.1015408.
58. Meirer, F., Liu, Y., Pouyet, E., Fayard, B., Cotte, M., Sanchez, C., Andrews, J.C., Mehta, A., and Sciau, P. (2013). Full-field XANES analysis of Roman ceramics to estimate firing conditions—a novel probe to study hierarchical heterogeneous materials. J. Anal. At. Spectrom. *28*, 1870–1883. https://doi.org/10.1039/C3JA50226K.
59. Primpke, S., Wirth, M., Lorenz, C., and Gerdts, G. (2018). Reference database design for the automated analysis of microplastic samples based on Fourier transform infrared (FTIR) spectroscopy. Anal. Bioanal. Chem. *410*, 5131–5141. https://doi.org/10.1007/s00216-018-1156-x.
60. Mak, R., Lerotic, M., Fleckenstein, H., Vogt, S., Wild, S.M., Leyffer, S., Sheynkin, Y., and Jacobsen, C. (2014). Non-negative matrix analysis for effective feature extraction in X-ray spectromicroscopy. Faraday Discuss. *171*, 357–371. https://doi.org/10.1039/C4FD00023D.
61. Li, Y., Zhang, K., Zheng, B., and Yang, F. (2016). Effect of local deformation on the coupling between diffusion and stress in lithium-ion battery. Int. J. Solids Struct. *87*, 81–89. https://doi.org/10.1016/j.ijsolstr.2016.02.029.
62. Balakrishna, A.R. (2022). Crystallographic design of intercalation materials. https://doi.org/10.48550/arXiv.2204.04525.
63. Rezaei, S., Asheri, A., and Xu, B.X. (2021). A consistent framework for chemo-mechanical cohesive fracture and its application in solid-state batteries. J. Mech. Phys. Solids *157*, 104612. https://doi.org/10.1016/j.jmps.2021.104612.
64. Shapiro, D.A., Yu, Y.S., Tyliszczak, T., Cabana, J., Celestre, R., Chao, W., Kaznatcheev, K., Kilcoyne, A.L.D., Maia, F., Marchesini, S., et al. (2014). Chemical composition mapping with nanometre resolution by soft X-ray microscopy. Nat. Photonics *8*, 765–769. https://doi.org/10.1038/nphoton.2014.207.
65. Fraggedakis, D., Nadkarni, N., Gao, T., Zhou, T., Zhang, Y., Han, Y., Stephens, R.M., Shao-Horn, Y., and Bazant, M.Z. (2020). A scaling law to determine phase morphologies during ion intercalation. Energy Environ. Sci. *14*, 112. https://doi.org/10.1039/D0EE00653J.
66. Wang, J., and Li, J.H. (2022). Scanning transmission X-ray microscopy at the Canadian light source: progress and selected applications in geosciences. At. Spectrosc. *43*, 84–98. https://doi.org/10.46770/AS.2022.008.
67. Olivo, A., and Robinson, I. (2014). Taking X-ray phase contrast imaging into mainstream applications and its satellite workshop Real and reciprocal space X-ray imaging. Phil. Trans. Math. Phys. Eng. Sci. *372*. https://doi.org/10.1098/rsta.2013.0359.
68. Takahashi, Y., Suzuki, A., Furutaku, S., Yamauchi, K., Kohmura, Y., and Ishikawa, T. (2013). High-resolution and high-sensitivity phase-contrast imaging by focused hard x-ray ptychography with a spatial filter. Appl. Phys. Lett. *102*, 094102. https://doi.org/10.1063/1.4794063.

69. de Jesus, L.R., Zhao, Y., Horrocks, G.A., Andrews, J.L., Stein, P., Xu, B.-X.B., and Banerjee, S. (2017). Lithiation across interconnected $V_2O_5$ nanoparticle networks. J. Mater. Chem. *5*, 20141–20152. https://doi.org/10.1039/C7TA04892K.

70. Basak, S., Migunov, V., Tavabi, A.H., George, C., Lee, Q., Rosi, P., Arszelewska, V., Ganapathy, S., Vijay, A., Ooms, F., et al. (2020). Operando transmission electron microscopy study of all-solid-state battery interface: redistribution of lithium among interconnected particles. ACS Appl. Energy Mater. *3*, 5101–5106. https://doi.org/10.1021/acsaem.0c00543.

71. Delmas, C., Maccario, M., Croguennec, L., le Cras, F., and Weill, F. (2008). Lithium deintercalation in LiFePO4 nanoparticles via a domino-cascade model. Nat. Mater. *7*, 665–671. https://doi.org/10.1038/nmat2230.

72. Robert, D., Douillard, T., Boulineau, A., Brunetti, G., Nowakowski, P., Venet, D., Bayle-Guillemaud, P., and Cayron, C. (2013). Multiscale phase mapping of LiFePO4-based electrodes by transmission electron microscopy and electron forward scattering diffraction. ACS Nano *7*, 10887–10894. https://doi.org/10.1021/nn4043964.

73. Boesenberg, U., Meirer, F., Liu, Y., Shukla, A.K., Dell'Anna, R., Tyliszczak, T., Chen, G., Andrews, J.C., Richardson, T.J., Kostecki, R., et al. (2013). Mesoscale phase distribution in single particles of LiFePO4 following lithium deintercalation. Chem. Mater. *25*, 1664–1672. https://doi.org/10.1021/cm400106k.

74. Satto, C., Sciau, P., Dooryhee, E., Galy, J., and Millet, P. (1999). The $\delta \rightarrow \varepsilon \rightarrow \gamma$ $LiV_2O_5$ "high temperature" phase transitions evidenced by synchrotron X-ray powder diffraction analysis. J. Solid State Chem. *146*, 103–109. https://doi.org/10.1006/jssc.1999.8314.

75. Li, Y., el Gabaly, F., Ferguson, T.R., Smith, R.B., Bartelt, N.C., Sugar, J.D., Fenton, K.R., Cogswell, D.A., Kilcoyne, A.L.D., Tyliszczak, T., et al. (2014). Current-induced transition from particle-by-particle to concurrent intercalation in phase-separating battery electrodes. Nat. Mater. *13*, 1149–1156. https://doi.org/10.1038/nmat4084.

76. Meethong, N., Huang, H.Y.S., Speakman, S.A., Carter, W.C., and Chiang, Y.M. (2007). Strain accommodation during phase transformations in olivine-based cathodes as a materials selection criterion for high-power rechargeable batteries. Adv. Funct. Mater. *17*, 1115–1123. https://doi.org/10.1002/adfm.200600938.

77. Omenya, F., Chernova, N.A., Zhang, R., Fang, J., Huang, Y., Cohen, F., Dobrzynski, N., Senanayake, S., Xu, W., and Whittingham, M.S. (2013). Why substitution enhances the reactivity of LiFePO4. Chem. Mater. *25*, 85–89. https://doi.org/10.1021/cm303259j.

78. Ferraro, M.E., Trembacki, B.L., Brunini, V.E., Noble, D.R., and Roberts, S.A. (2020). Electrode mesoscale as a collection of particles: coupled electrochemical and mechanical analysis of NMC cathodes. J. Electrochem. Soc. *167*, 013543. https://doi.org/10.1149/1945-7111/ab632b.

79. Zhang, X., van Hulzen, M., Singh, D.P., Brownrigg, A., Wright, J.P., van Dijk, N.H., and Wagemaker, M. (2015). Direct view on the phase evolution in individual LiFePO4 nanoparticles during Li-ion battery cycling. Nat. Commun. *6*, 1–7. https://doi.org/10.1038/ncomms9333.

80. Zhang, Y., Luo, Y., Fincher, C., Banerjee, S., and Pharr, M. (2019). Chemo-mechanical degradation in $V_2O_5$ thin film cathodes of Li-ion batteries during electrochemical cycling. J. Mater. Chem. A Mater. *7*, 23922–23930. https://doi.org/10.1039/C9TA05243G.

81. Mistry, A., Usseglio-Viretta, F.L.E., Colclasure, A., Smith, K., and Mukherjee, P.P. (2020). Fingerprinting redox heterogeneity in electrodes during extreme fast charging. J. Electrochem. Soc. *167*, 090542. https://doi.org/10.1149/1945-7111/ab8fd7.

82. Lin, B., Emami, N., Santos, D.A., Luo, Y., Banerjee, S., and Xu, B.-X. (2022). A deep learned nanowire segmentation model using synthetic data augmentation. npj Comput. Mater. *8*, 1–12. https://doi.org/10.1038/s41524-022-00767-x.

83. Zhao, Y., de Jesus, L.R., Stein, P., Horrocks, G.A., Banerjee, S., and Xu, B.X. (2017). Modeling of phase separation across interconnected electrode particles in lithium-ion batteries. RSC Adv. *7*, 41254–41264. https://doi.org/10.1039/c7ra07352f.

84. Deng, H.D., Zhao, H., Jin, N., Hughes, L., Savitzky, B.H., Ophus, C., Fraggedakis, D., Borbély, A., Yu, Y.-S., Lomeli, E.G., et al. (2022). Correlative image learning of chemo-mechanics in phase-transforming solids. Nat. Mater. *2022*, 1–8. https://doi.org/10.1038/s41563-021-01191-0.

85. Muralidharan, N., Brock, C.N., Cohn, A.P., Schauben, D., Carter, R.E., Oakes, L., Walker, D.G., and Pint, C.L. (2017). Tunable mechanochemistry of lithium battery electrodes. ACS Nano *11*, 6243–6251. https://doi.org/10.1021/acsnano.7b02404.

86. Muralidharan, N., Carter, R., Oakes, L., Cohn, A.P., and Pint, C.L. (2016). Strain engineering to modify the electrochemistry of energy storage electrodes. Sci. Rep. *6*, 1–9. https://doi.org/10.1038/srep27542.

87. Zhang, D., Sheth, J., Sheldon, B.W., and Renuka Balakrishna, A. (2021). Film strains enhance the reversible cycling of intercalation electrodes. J. Mech. Phys. Solids *155*, 104551. https://doi.org/10.1016/j.jmps.2021.104551.

88. Suthirakun, S., Jungthawan, S., and Limpijumnong, S. (2018). Effect of Sn-doping on behavior of Li-intercalation in $V_2O_5$ cathode materials of Li-ion batteries: a computational perspective. J. Phys. Chem. C *122*, 5896–5907. https://doi.org/10.1021/acs.jpcc.7b12321.

89. Moura, S.J., Chaturvedi, N.A., and Krstic, M. (2012). PDE estimation techniques for advanced battery management systems Part II: SOH identification. Proc. Am. Control Conf. 566–571. https://doi.org/10.1109/ACC.2012.6315019.

90. Khayamy, M., Nasiri, A., and Okoye, O. (2020). Development of an equivalent circuit for batteries based on a distributed impedance network. IEEE Trans. Veh. Technol. *69*, 6119–6128. https://doi.org/10.1109/TVT.2020.2989715.

91. Toby, B.H., and von Dreele, R.B. (2013). GSAS-II: the genesis of a modern open-source all purpose crystallography software package. J. Appl. Crystallogr. *46*, 544–549. https://doi.org/10.1107/S0021889813003531.

92. Virtanen, P., Gommers, R., Oliphant, T.E., Haberland, M., Reddy, T., Cournapeau, D., Burovski, E., Peterson, P., Weckesser, W., Bright, J., et al. (2020). SciPy 1.0: fundamental algorithms for scientific computing in Python. Nat. Methods *17*, 261–272. https://doi.org/10.1038/s41592-019-0686-2.